Doctoral dissertation

<AY2023>

Study on Electrolytes and Separators for High Energy Density Rechargeable Batteries with Lithium Metal Anode

（リチウム金属負極を用いた高エネルギー密度二次電池用電解液およびセパレータに関する研究）

Yuma Shimbori

Graduate School of Urban Environmental Sciences

Tokyo Metropolitan University

Preface

Firstly, the studies were conducted under the supervision of Professor Kiyoshi Kanamura at the Department of Applied Chemistry for Environment, Faculty of Urban Environmental Sciences, Tokyo Metropolitan University. The author would like to acknowledge Prof. Kiyoshi Kanamura for his enormous supports and insightful suggestions.

The author also thanks Supervisor, Professor Koichi Kajihara at the Department of Applied Chemistry for Environment, Graduate School of Urban Environmental Sciences, Tokyo Metropolitan University, for his special advice and support. I would like to express sincere gratitude to Professor Takashi Yanagishita and Associate Professor Manabu Tanaka at the Department of Applied Chemistry for Environmental, Graduate School of Urban Environmental Sciences, Tokyo Metropolitan University for their helpful comments.

I would like to show my appreciation to Assistant Professor Hirokazu Munakata and Assistant Professor Masanao Ishijima at the Department of Applied Chemistry for Environmental, Graduate School of Urban Environmental Sciences, Tokyo Metropolitan University. They publicly and personally helped me.

My deepest appreciation goes to all the members of Kanamura, Kajihara, and Yanagishita laboratories for their enormous support during my study.

Finally, I would like to express my gratitude to my family, Tomoyuki Shimbori, Koko Shimbori, and Fumiya Shimbori for their moral support and warm encouragement.

March 2024

Contents

Chapter 1: General introduction

1.1. Introduction

A consumption of fossil fuels, such as coal, oil, and natural gas, is a serious concern for resource depletion and a generation of greenhouse gases that contribute to global warming. Therefore, an introduction of various alternative clean energy sources, such as geothermal energy, hydroelectric energy, wind power energy, solar energy, and nuclear power energy has been required to reduce greenhouse gas emissions. Since these energies are converted into an electrical energy, both electrical energy transport and storage are very important. Recently, energy devices for electrical energy storage have been widely researched. There are some kinds of energy storage devices. Among these devices, rechargeable batteries, such as lead-acid, nickel-cadmium, redox flow, and Li-ion batteries (LIBs) have been more extensively applied to energy storage systems.[1]

The performance of the rechargeable battery is evaluated by various parameters, such as a gravimetric or volumetric energy density, a rate capability, a cycle performance, a cost, and a safety.[2] Among various rechargeable batteries, LIBs achieve the highest energy densities (150–200 Wh kg^{-1}, 300–400 Wh L^{-1}), as shown in Fig. 1-1.[3–5] The energy density of rechargeable batteries is highly dependent on the electrode active materials. In LIBs, $LiCoO_2$, $LiNi_xCo_yMn_zO_2$ (x+y+z=1), $LiFePO_4$, etc. have been used as a cathode material, and graphite (LiC_6) or $Li_4Ti_5O_{12}$ has been used as an anode material.[3,6–10] Recently, the energy density of LIBs has been approaching the theoretical upper limit. But, new demands for higher energy densities are claimed. Therefore, next-generation batteries (post-LIBs) employing different electrode active materials from LIBs, such as Sulfur, Oxygen in air, silicon, and Li metal have been studied. Particularly, Li metal anode

is a key technology for various next-generation batteries, for example, Li-S, Li-air, and Li-metal batteries (LMBs).[2,3,5]

1.2. Li-metal anode

Figures 1-2 (a) and (b) show both configurations of LIBs with graphite anode and LMBs with Li metal anode. The charge–discharge process of graphite anode is an intercalation reaction in the following Eq. 1-1 and that of Li-metal anode is a deposition/dissolution reaction in the following Eq. 1-2.

$$C_6 + xLi + xe^- \rightleftarrows Li_xC_6 \quad (1\text{-}1)$$

$$Li \rightleftarrows Li^+ + e^- \quad (1\text{-}2)$$

The Li-metal anode provides a theoretical capacity (3860 mAh g^{-1}) that is 10 times higher than the theoretical capacity of graphite (372 mAh g^{-1}), as shown in Fig. 1-3.[3] Furthermore, the Li-metal anode can provide a higher operation voltage of the cell owing to the lowest redox potential (–3.04 V vs. SHE).[3] Based on these properties, it can be said that Li metal is an ideal anode material attracting much attention as a promising anode material for various next-generation batteries.

However, achieving a uniform reaction of the Li-metal anode is not so easy. Nonuniform reaction distribution on the electrodes results in nonuniform Li deposition promoting an internal short circuit. The nonuniform Li deposition breaks a solid electrolyte interphase (SEI) layer, promoting an electrolyte decomposition.[11–13] The electrolyte decomposition results in a decrease in coulombic efficiency and cycle performance. Furthermore, the internal short circuit also results in low coulombic efficiency and sometimes a thermal runaway of the cell.

Various approaches have been investigated to solve these problems. Firstly, a control of size and morphology for Li deposits have been investigated by an external pressure and a selection of proper electrolytes. [14–18] Larger Li deposits have a smaller surface area, which prevents depletion of electrolytes by chemical reactions between Li and electrolyte and a decrease in coulombic efficiency. Granular deposits have a smaller surface area than those of mossy and dendritic Li deposits, leading to a lower risk of internal short circuit through a separator between the anode and cathode. Another important approach for an establishment of uniform reaction for Li metal anode is the optimization of the SEI layer composition determined by both kinds of electrolytes and additives.[13,19–26] A high mechanical strength of the SEI layer suppresses the undesirable reactions between electrolyte and Li metal. In other words, a more physically stable and uniform SEI layer provides a higher coulombic efficiency owing to the suppression of electrolyte decomposition and the more uniform distribution of electrode reactions.[11–13,27] Some studies on an artificial SEI consisting of polymer electrolytes, ceramic materials, etc. have been conducted to obtain a more stable SEI layer on Li metal.[28–34] The most important point in real cells is the uniformity of current distribution, including a porous polymer separator.[35–39] The separator directly contributes to the current distribution (reaction distribution on the electrode). Therefore, the pore structure of the separator greatly affected the reaction distribution in the cathode and anode layers. The separators with appropriate pore structures provide uniform reaction distribution.

1.3. Electrolytes

Since the redox potential of Li metal is very low (–3.04 V vs. SHE), the electrolytes should have a high reduction stability. This is the first priority for the

requirement of electrolytes employed in LMBs. [40] Other requirements are a high ionic conductivity, a high thermal stability, and a high safety. So far, some organic electrolyte solvents, ionic liquid electrolytes (ILEs), and gel polymer electrolytes (GPEs) have been investigated as electrolytes of LMBs.

1.3.1. Organic electrolyte solution

Organic electrolyte solutions are prepared by dissolving Li salts in nonprotic organic solvents. [40] Cyclic carbonates, such as propylene carbonate (PC) and ethylene carbonate (EC), have been sometimes selected for nonprotic organic solvents because of their higher redox stability and Li salt solubility.[41–44] Linear carbonates, such as dimethyl carbonate (DMC), diethyl carbonate (DEC), and ethyl methyl carbonate (EMC), are usually added to reduce both freezing point and viscosity. [45–48] Li salts are highly soluble in solvents and easily dissociate with ions. $LiPF_6$, $LiClO_4$, $LiBF_4$, $LiB(C_2O_4)_2$ (Li bis(oxalate)borate, LiBOB), $LiN(C_2F_4SO_2)_2$ (Li bis(trifluoromethanesulfonyl)imide, LiTFSI), and $LiN(CF_3SO_2)_2$ (Li bis(fluorosulfonyl)imide, LiFSI) are promising candidates.[45,49–53] In most cases, $LiPF_6$ is selected because of its high redox stability, high thermal stability, high safety, low cost, and high compatibility to anode.

Recently, highly concentrated electrolytes in which Li salts are dissolved at high concentrations (higher than 3 mol dm^{-3}) have been attracting attention. Solvent-shared ion pairs (SSIP) are preferentially formed in dilute salt concentration (lower than 1 mol dm^{-3}) electrolytes, while contact ion pairs (CIP) and aggregates (AGG) of CIP are formed in highly concentrated electrolytes.[54–56] Highly concentrated electrolytes exhibit higher ionic conductivity, higher Li^+ ion transport number, wider electrochemical potential window, and flame-retardancy owing to a unique solvent structure.

Since the reduction potential of electrolytes is more positive than that of anode materials, the electrolytes undergo a reductive decomposition on the anode. However, the decomposition products of the electrolytes are deposited to form a surface film on the anode, suppressing direct contact between the electrolyte and the anode. This film is defined as the SEI layer, and its composition and thickness are very important parameters for anode performance.[57] Additives, such as fluoroethylene carbonate (FEC) and 1,3-propane sultone (PS), have been added to the electrolyte solutions to support a formation of functional SEI layer.[22–24,58–60] These additives are reductively decomposed at more positive potential than that of the electrolytes to form a well-composed SEI layer.

1.3.2. Ionic liquid electrolyte

ILs are salts in a liquid state. ILEs composed of ions without any solvents have lower melting points than room temperature and unique properties, such as negligible volatility and nonflammable. Therefore, an introduction of ILEs in LMBs can improve the battery safety. Physical properties of ILEs, such as ionic conductivity and electrochemical potential window, can be controlled by appropriate selection of the cations and anions. So far, pyrrolidinium, imidazolium, ammonium, and phosphonium-based cation species, and TFSI and FSI anion species have been investigated, and these observations indicated that FSI anion significantly improves the battery performance.[15,61–67] Highly concentrated electrolytes of ILEs, as well as organic electrolytes, have provided better performance.

1.3.3. Gel polymer electrolyte

Gel polymer electrolytes (GPEs) with supporting electrolyte solutions added to

polymers are classified into homogeneous and heterogeneous types. In the homogeneous type, the polymer and electrolytes are in a homogeneous phase, and polyethylene oxide (PEO) is a typical polymer. In the heterogeneous type, a crystalline part of polymer forms the polymer framework, and the amorphous parts between the crystalline networks are gelated by the electrolyte solutions. GPEs can improve battery safety and simplify cell fabrication owing to a lower electrolyte leakage. GPE can also use ILEs as the supporting electrolytes, which is defined as an ion gel (IG).[68–71] However, the ionic conductivity of GPEs is usually lower than that of the electrolyte solutions, because of an interference of ionic conduction by polymer.

1.4. Separators

A main role of the separator is a separation between the cathode and anode to avoid an internal short circuit in a cell. However, a separator is a very important component that holds an electrolyte and establishes an ion conduction pathway between cathode and anode. Therefore, a separator greatly affects an electrode reaction and a battery performance. Nonuniform reaction (nonuniform current flow) distribution on an electrode promotes an electrode active material degradation and a nonuniform Li deposition in LMBs. In other words, a battery performance can be improved by employing an appropriate separator. The requirements for separators are not only material properties, such as high chemical stability, high thermal stability, high mechanical strength, high affinity with electrolytes, and high gas permeability, but also an optimized pore structures, such as porosity, pore diameter, and pore shape.[36,72–74] In particular, the pore structure strongly depends on the preparation process for separators. Generally, the separators with a thickness of 10–30 μm are required to realize high power and energy

densities of cells.

1.4.1. Polyolefin (microporous) separators

Polyolefin separators are the most conventional separators and are microporous membranes with submicron pores. They are prepared by two types of processes: dry process and wet process.[72–74] The pore structure of these membranes is nonuniform owing to the separator preparation process. Theie electrolyte retention capability is low owing to their low porosity and low affinity with electrolytes. These properties reduce an apparent ionic conductivity of a separator part. Some polyolefin separators are surfactant-coated to improve affinity with electrolytes, but an effect of surfactants on battery properties is concerned.[35,36] Recently, ceramic-coated polyolefin separators have been developed to improve an affinity with electrolytes, thermal stability, and internal short-circuit resistance for Li dendrite.[36,75,76]

1.4.2. Nonwoven separators

Nonwoven membranes have been also investigated as alternative separators owing to their highly interconnected pore structures. Nonwoven separators exhibit higher ionic conductivities owing to their higher porosity and open pore structures compared with those of polyolefin separators.[77] The preparation process includes a wet- or dry-laid process, melt-blowing process, and electrospinning process. [36,74] These processes make it possible to employ materials with higher thermal stability and higher affinity with electrolytes. So far, polyester, polyamide, and polyimide (PI) have been used as polymer matrix of nonwoven separators. However, the pore size is as large as several tens of micrometers, leading to an internal short circuit by Li dendrite formation.

1.4.3. 3DOM separator

The three-dimensionally ordered macroporous (3DOM) separator is a membrane with a quasi-inverse opal structure. The 3DOM separator has a high porosity of approximately 74% and an interconnected pore structure.[78,79] Figure 1-4 shows the 3DOM (inverse opal) structure. The 3DOM structure can provide a uniform ion flux inside the separator and reaction (current flow) distribution on the electrode. Furthermore, it achieves a high chemical and thermal stability by using engineering plastics as polymer materials.[37–39,80]

1.5. Outline of dissertation

In this dissertation, rechargeable Li batteries (LMB with oxide cathode and Li-S battery) were realized by using the 3DOM separator and highly concentrated electrolytes.

In Chapter 2, LMBs employing highly concentrated ILEs were studied. Both high viscosity and high polarity of highly concentrated ILEs limits the type of separator that can be used in LMBs. Therefore, surfactant-coated PP and 3DOM PI separators were employed to construct LMBs. These LMBs were compared to understand an effect of separator on battery performance of LMBs.

In Chapter 3, LMBs employing IG were investigated. IG can suppress an electrolyte leakage which contribute an improvement of battery safety and also simplify a cell fabrication. However, IG has a low mechanical strength. A thick IG can only be applied to batteries. This decreases an energy density of battery. In this study, the 3DOM PI and IG were combined to prepare a thin IG separator and evaluated the battery performances with the composite membrane.

In Chapter 4, the mechanical strength of the 3DOM separator was investigated to improve a cyclability of LMBs. The 3DOM PI separator has been made of PI. The mechanical strength is not enough to obtain long cycle performance of LMBs. Therefore, the 3DOM separator with higher mechanical strength is required. In this study, 10 wt.% of polybenzimidazole (PBI) was added to PI and compared to understand an effect of mechanical strength of separator on battery performance of LMBs.

In Chapter 5, Li-Sulfur batteries with the 3DOM PI separator were investigated, as one of applications. Although the dissolution of discharge intermediates can be suppressed by using an oxide-based solid electrolyte, an internal short circuit caused by the Li-metal anode took place. Therefore, the 3DOM PI separator was introduced with highly concentrated electrolytes between the electrolyte and anode interface to improve the performance of Li-Sulfur batteries with solid electrolytes.

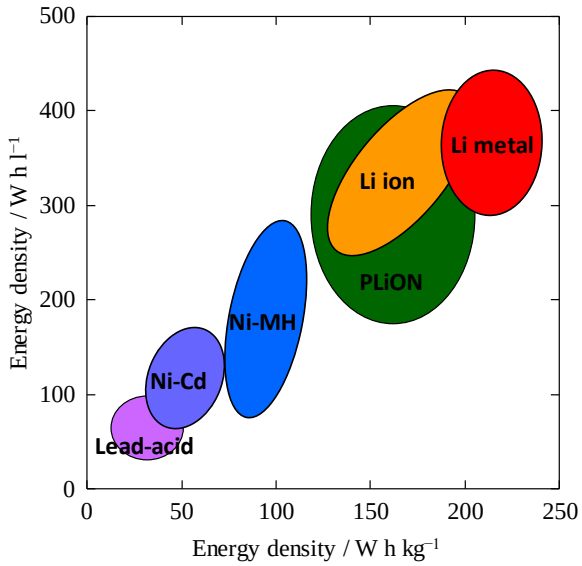

Figure 1–1. Schematic illustration of energy density of various rechargeable batteries.

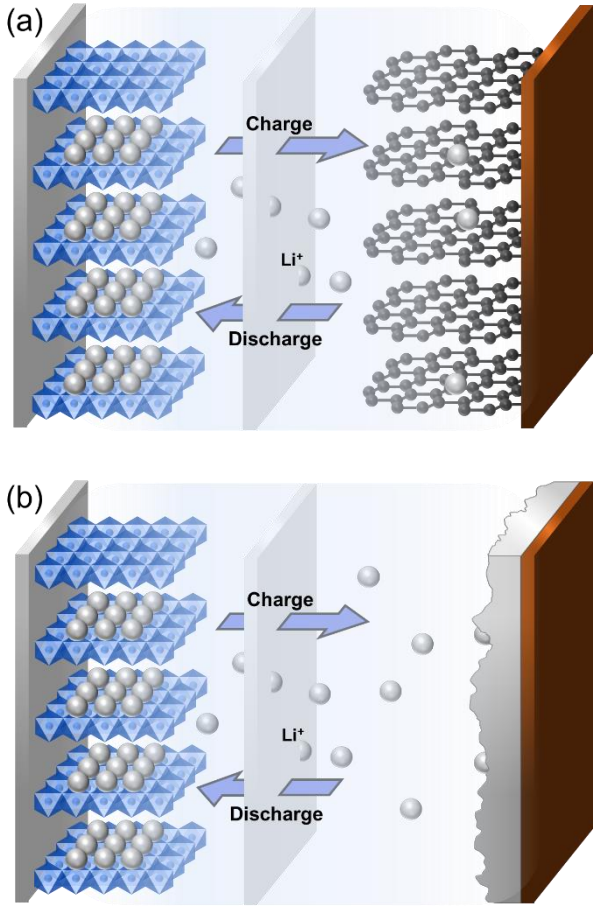

Figures 1–2. Configurations of (a) LIBs with graphite anode and (b) LMBs with Li metal anode.

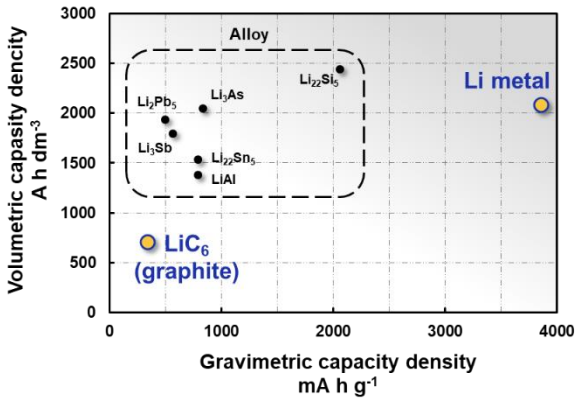

Figure 1–3. Specific capacity density of anode materials for lithium-ion batteries.

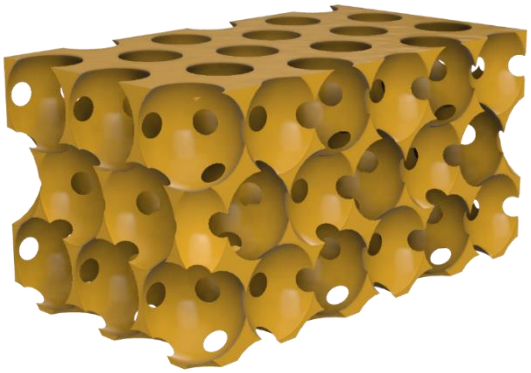

Figure 1–4. Schematic illustration of 3DOM structure.

1.6. References

1. M. Armand, and J. M. Tarascon, Nature, 451, 652 (2008)
2. A. El Kharbachi, O. Zavorotynska, M. Latroche, F. Cuevas, V. Yartys, and M. Fichtner, J. Alloys Compd., 817, 153261 (2020)
3. J. M. Tarascon, and M. Armand, Nature, 414, 359 (2001)
4. M. Ue, and K. Uosaki, Curr. Opin. Electrochem., 17, 106 (2019)
5. M. Ue, K. Sakaushi, and K. Uosaki, Materials Horizons, 7, 1937 (2020)
6. K. Mizushima, P. C. Jones, P. J. Wiseman, and J. B. Goodenough, Mater. Res. Bull., 15, 783 (1980)
7. T. Ohzuku, and Y. Makimura, Chem. Lett., 30, 642 (2001)
8. N. Yabuuchi, and T. Ohzuku, J. Power Sources, 119-121, 171 (2003)
9. A. K. Padhi, K. S. Nanjundaswamy, and J. B. Goodenough, J. Electrochem. Soc., 144, 1188 (1997)
10. K. M. Colbow, J. R. Dahn, and R. R. Haering, J. Power Sources, 26, 397 (1989)
11. Y. S. Cohen, Y. Cohen, and D. Aurbach, J. Phys. Chem. B, 104, 12282 (2000)
12. W. Xu, J. L. Wang, F. Ding, X. L. Chen, E. Nasybutin, Y. H. Zhang, and J. G. Zhang, Energy Environ. Sci., 7, 513 (2014)
13. H. P. Wu, H. Jia, C. M. Wang, J. G. Zhang, and W. Xu, Adv. Energy Mater., 11, 2003092 (2021)
14. S. Kanamori, M. Matsumoto, S. Taminato, D. Mori, Y. Takeda, H. J. Hah, T. Takeuchi, and N. Imanishi, Rsc Advances, 10, 17805 (2020)
15. J. Hwang, H. Okada, R. Haraguchi, S. Tawa, K. Matsumoto, and R. Hagiwara, J. Power Sources, 453 (2020)
16. X. Shen, R. Zhang, P. Shi, X. Chen, and Q. Zhang, Adv. Energy Mater., 11,

2003416 (2021)

17. C. C. Fang, B. Y. Lu, G. Pawar, M. H. Zhang, D. Y. Cheng, S. R. Chen, M. Ceja, J. M. Doux, H. Musrock, M. Cai, B. Liaw, and Y. S. Meng, Nat. Energy, 6, 987 (2021)

18. R. Furuya, T. Hara, T. Fukunaga, K. Kawakami, N. Serizawa, and Y. Katayama, J. Electrochem. Soc., 168, 100516 (2021)

19. S. Shiraishi, K. Kanamura, and Z. Takehara, J. Appl. Electrochem., 25, 584 (1995)

20. K. Kanamura, S. Shiraishi, and Z. Takehara, J. Electrochem. Soc., 143, 2187 (1996)

21. K. Kanamura, S. Shiraishi, and Z. Takehara, J. Fluorine Chem., 87, 235 (1998)

22. R. Mogi, M. Inaba, S. K. Jeong, Y. Iriyama, T. Abe, and Z. Ogumi, J. Electrochem. Soc., 149, A1578 (2002)

23. X. Q. Zhang, X. B. Cheng, X. Chen, C. Yan, and Q. Zhang, Adv. Funct. Mater., 27, 1605989 (2017)

24. N. Piao, S. F. Liu, B. Zhang, X. Ji, X. L. Fan, L. Wang, P. F. Wang, T. Jin, S. C. Liou, H. C. Yang, J. J. Jiang, K. Xu, M. A. Schroeder, X. M. He, and C. S. Wang, ACS Energy Letters, 6, 1839 (2021)

25. X. Wang, W. Zeng, L. Hong, W. W. Xu, H. K. Yang, F. Wang, H. G. Duan, M. Tang, and H. Q. Jiang, Nat. Energy, 3, 227 (2018)

26. Y. Maeyoshi, K. Yoshii, and H. Sakaebe, Electrochemistry, 90, 047001 (2022)

27. C. Hou, J. H. Han, P. Liu, C. C. Yang, G. Huang, T. Fujita, A. Hirata, and M. W. Chen, Adv. Energy Mater., 9, 1902675 (2019)

28. J. W. Meng, F. L. Chu, J. L. Hu, and C. L. Li, Adv. Funct. Mater., 29, 1902220 (2019)

29. F. Liu, Q. F. Xiao, H. B. Wu, L. Shen, D. Xu, M. Cai, and Y. F. Lu, Adv. Energy Mater., 8, 1701744 (2018)

30. C. Wu, F. H. Guo, L. Zhuang, X. P. Ai, F. P. Zhong, H. X. Yang, and J. F. Qian, ACS Energy Letters, 5, 1644 (2020)

31. L. Y. Chen, J. W. Lai, Z. L. Li, H. Q. Zou, J. H. Yang, K. Ding, Y. P. Cai, and Q. F. Zheng, Communications Materials, 4 (2023)

32. Y. Y. Liu, D. C. Lin, P. Y. Yuen, K. Liu, J. Xie, R. H. Dauskardt, and Y. Cui, Adv. Mater., 29, 1605531 (2017)

33. H. Y. Dong, X. L. Xiao, C. Jin, X. R. Wang, P. P. Tang, C. B. Wang, Y. H. Yin, D. Wang, S. T. Yang, and C. Wu, J. Power Sources, 423, 72 (2019)

34. R. Xu, X. Q. Zhang, X. B. Cheng, H. J. Peng, C. Z. Zhao, C. Yan, and J. Q. Huang, Adv. Funct. Mater., 28, 1705838 (2018)

35. C. F. J. Francis, I. L. Kyratzis, and A. S. Best, Adv. Mater., 32, 1904205 (2020)

36. J. Jang, J. Oh, H. Jeong, W. Kang, and C. Jo, Materials, 13, 4625 (2020)

37. Y. Maeyoshi, S. Miyamoto, H. Munakata, and K. Kanamura, J. Power Sources, 350, 103 (2017)

38. Y. Shimizu, and K. Kanamura, J. Electrochem. Soc., 166, A754 (2019)

39. J. Takeyoshi, N. Kobori, and K. Kanamura, Electrochemistry, 88, 540 (2020)

40. K. Xu, Chem. Rev., 104, 4303 (2004)

41. R. Selim, and P. Bro, Journal of Electrochemical Society, 121, 1457 (1974)

42. R. D. Rauh, and S. B. Brummer, Electrochimica Acta, 22, 75 (1977)

43. G. Pistoia, M. De Rossi, and B. Scrosati, J. Electrochem. Soc., 117, 500 (1970)

44. R. Fong, U. v. Sacken, and J. R. Dahn, 137, 2009 (1990)

45. J. M. Tarascon, and D. Guyomard, Solid State Ionics, 69, 293 (1994)

46. D. Guyomard, and J. M. Tarascon, J. Electrochem. Soc., 140, 3071 (1993)

47. D. Aurbach, A. Zaban, A. Schechter, Y. Eineli, E. Zinigrad, and B. Markovsky, J. Electrochem. Soc., 142, 2873 (1995)

48. Y. Ein-Eli, S. R. Thomas, V. Koch, D. Aurbach, B. Markovsky, and A. Schechter, J. Electrochem. Soc. (1996)

49. J. R. Dahn, U. von Sacken, M. W. Juzkow, and H. Al-Janaby, J. Electrochem. Soc., 138, 2207 (1991)

50. A. Abouimrane, J. Ding, and I. J. Davidson, J. Power Sources, 189, 693 (2009)

51. H. B. Han, S. S. Zhou, D. J. Zhang, S. W. Feng, L. F. Li, K. Liu, W. F. Feng, J. Nie, H. Li, X. J. Huang, M. Armand, and Z. B. Zhou, J. Power Sources, 196, 3623 (2011)

52. W. Xu, and C. A. Angell, Electrochemical and Solid State Letters, 4, E1 (2001)

53. K. Xu, S. S. Zhang, T. R. Jow, W. Xu, and C. A. Angell, Electrochemical and Solid State Letters, 5, A26 (2002)

54. Y. Yamada, and A. Yamada, J. Electrochem. Soc., 162, A2406 (2015)

55. Y. Yamada, J. H. Wang, S. Ko, E. Watanabe, and A. Yamada, Nat. Energy, 4, 269 (2019)

56. S. Ko, T. Obukata, T. Shimada, N. Takenaka, M. Nakayama, A. Yamada, and Y. Yamada, Nat. Energy, 7, 1217 (2022)

57. E. Peled, J. Electrochem. Soc., 126, 2047 (1979)

58. E. G. Leggesse, and J. C. Jiang, Rsc Advances, 2, 5439 (2012)

59. B. Zhang, M. Metzger, S. Solchenbach, M. Payne, S. Meini, H. A. Gasteiger, A. Garsuch, and B. L. Lucht, J. Phys. Chem. C, 119, 11337 (2015)

60. X. X. Zuo, M. Q. Xu, W. S. Li, D. G. Su, and J. S. Liu, Electrochemical and Solid

State Letters, 9, A196 (2006)

61. Y. S. Fung, and R. Q. Zhou, J. Power Sources, 81-82, 891 (1999)

62. H. Sakaebe, and H. Matsumoto, Electrochem. Commun., 5, 594 (2003)

63. H. Sano, H. Sakaebe, and H. Matsumoto, J. Power Sources, 196, 6663 (2011)

64. A. Lewandowski, and A. Świderska-Mocek, J. Power Sources, 194, 601 (2009)

65. M. Watanabe, M. L. Thomas, S. Zhang, K. Ueno, T. Yasuda, and K. Dokko, Chem Rev, 117, 7190 (2017)

66. G. M. A. Girard, M. Hilder, H. Zhu, D. Nucciarone, K. Whitbread, S. Zavorine, M. Moser, M. Forsyth, D. R. MacFarlane, and P. C. Howlett, Physical Chemistry Chemical Physics, 17, 8706 (2015)

67. T. Pathirana, R. Kerr, M. Forsyth, and P. C. Howlett, J. Electrochem. Soc., 167 (2020)

68. M. Freemantle, Chem. Eng. News, 82, 26 (2004)

69. M. A. Susan, T. Kaneko, A. Noda, and M. Watanabe, Journal of the American Chemical Society, 127, 4976 (2005)

70. S. Seki, A. B. H. Susan, T. Kaneko, H. Tokuda, A. Noda, and M. Watanabe, J. Phys. Chem. B, 109, 3886 (2005)

71. X. W. Li, Y. W. Zheng, and C. Y. Li, Energy Storage Materials, 29, 273 (2020)

72. P. Arora, and Z. M. Zhang, Chem. Rev., 104, 4419 (2004)

73. S. S. Zhang, J. Power Sources, 164, 351 (2007)

74. X. S. Huang, J. Solid State Electrochem., 15, 649 (2011)

75. H. Lee, M. Yanilmaz, O. Toprakci, K. Fu, and X. W. Zhang, Energy Environ. Sci., 7, 3857 (2014)

76. J. Nunes-Pereira, C. M. Costa, and S. Lanceros-Méndez, J. Power Sources, 281,

378 (2015)

77. T. Evans, J. H. Lee, V. Bhat, and S. H. Lee, J. Power Sources, 292, 1 (2015)

78. H. Munakata, D. Yamamoto, and K. Kanamura, Chem. Commun., 3986 (2005)

79. K. Kanamura, T. Mitsui, and H. Munakata, Chem. Mater., 17, 4845 (2005)

80. M. Nagasaki, and K. Kanamura, ACS Appl. Energy Mater., 2, 3896 (2019)

Chapter 2: Application of 3DOM PI Separator to Li-Metal Battery with Highly Concentrated Ionic Liquid Electrolyte

2.1. Introduction

Lithium-ion batteries (LIBs) exhibit the highest energy density among the various practical rechargeable batteries. Recently, the energy density of rechargeable batteries has increased by employing active materials with higher-capacity densities. Li metal anode is the ultimate anode material owing to the theoretical capacity density of 3861 mAh g^{-1}, which is approximately 10 times larger than that of graphite anode (372 mAh g^{-1}). Moreover, the redox potential of Li metal anode is the lowest among all candidates of anode materials (–3.04 V vs. SHE).[1] Thus, lithium metal battery (LMB) using Li metal anode has been studied to realize batteries with higher energy densities. However, LMBs have critical problems such as poor safety and low cycle performance owing to an internal short circuit and low coulombic efficiency.[2–5] To overcome these challenges, alternative electrolytes with excellent safety properties are needed. Ionic liquid electrolytes (ILEs) are promising alternatives owing to their excellent properties including wide electrochemical potential window, negligible volatility, and high thermal stability.

The viscosity, electrochemical stability, and ionic conductivity of ILEs can be determined by the combinations of anions and cations. Thus, many combinations have been considered as electrolytes for LMBs.[6–12] In particular, pyrrolidinium-based ILEs have been reported as the best compromise between higher electrochemical stability and

higher ionic conductivity.[8–12] Furthermore, highly concentrated ILEs exhibit improved Li^+ transport number, rate capability, and cycle performance owing to their unique Li^+ conduction mechanism.[13–15]

The selection of the separator is another important factor when using ILEs for Li deposition/dissolution. The type of separator significantly affects the morphology of the Li metal deposited at the interface between the separator and the Li metal.[16–19] However, conventional polyolefin separators exhibit low affinity to ILEs and cannot be utilized for ILEs. Because of the lack of separators suitable for ILEs, a glass filter (thickness: 260 μm) has been used as an alternative separator in several previous studies.[7–11,15] In these reports, half cells with a low area capacity density cathode (1.0 mAh cm^{-2} or less) were employed in the dissolution/deposition cycle of Li metal anode. However, the effect of the separator on the Li deposition/dissolution cycle has not been thoroughly discussed. In cycle performance tests with high-area-capacity cathodes and ILEs, the separator plays an important role that significantly influences the cycle performance of the cell. Recently, Eftekharnia et al. conducted long-term cycling of $LiFePO_4$/Li cells with high area capacity cathode using two types of concentrated ILEs (*N*-methyl-*N*-propylpyrrolidinium bis(fluorosulfonyl)imide and triethyl(methyl)phosphonium bis(fluorosulfonyl)imide) and evaluated four representative conventional separators.[20] This study reported that the surfactant-coated polypropylene (PP) separator (Celgard®3000 series) exhibited the best results. This result was related to MacMullin number, pore size, and contact angle with these electrolytes. However, conventional separators, which have been optimized for LIBs with carbon anode, are unsuitable for Li metal deposition. Therefore, a new separator designed for Li-metal anodes must be developed to achieve Li deposition/dissolution with better reversibility in highly concentrated ILEs.

We developed an ultrafine porous polyimide membrane with an inverse opal structure.[21–24] This is three-dimensionally ordered macroporous polyimide (3DOM PI) separator that is applied to the Li metal anode to improve its cycle performance of the Li metal anode.[25–28] Li metal reacts with electrolytes to form a solid electrolyte interphase (SEI) with an inhomogeneous morphology and composition. This SEI results in an inhomogeneous Li^+ ion flux near the Li metal surface and Li deposition.[29] It has been reported that the 3DOM PI separator containing conventional organic electrolytes provides significantly better cycle performance of Li deposition/dissolution owning to its uniform structure generating a uniform Li^+ ion flux.[30–34]

In this study, we proposed a 3DOM PI separator for LMBs with highly concentrated ILEs. First, the affinity between the 3DOM PI separator and highly concentrated ILEs was confirmed. Subsequently, Li deposition/dissolution cycle tests were conducted to investigate the cycle performance of the Li metal anodes. Finally, the charge/discharge cycle test was performed using cells with $LiNi_{0.5}Co_{0.2}Mn_{0.3}O_2$ (NCM523, 2.0 mAh cm^{-2}) cathode and Li metal anode. The surfactant-coated PP separator was used as a standard polyolefin separator.

2.2. Experimental

2.2.1. Preparation of 3DOM PI separator

The 3DOM PI separator was prepared using a colloidal crystalline template method with mono-disperse silica particles. Polyamic acid (JVI-2002, JFE Chemical Corp.) and mono-disperse silica spherical particles (Seahostar, Nippon Shokubai Co., Ltd.) were used as the precursors for the polyimide and template particles, respectively. They were dispersed in *N*,*N*-dimethylacetamide (Wako Special Grade, Fujifilm Wako

Pure Panaca Co., Ltd.) to prepare a slurry. The slurry was coated on PET films (PANA-PEEL®NP-75-A, Panac Co., Ltd.) and thereafter dried to remove the solvent. The precursor sheet was imidizated by heating at 320 °C for 2 h. The silica particles remaining in the sheet were removed using a 10 wt% aqueous hydrofluoric acid solution. The resulting 3DOM PI was dried under vacuum at 120 °C for 48 h.

2.2.2. Preparation of the electrolyte

Lithium bis(fluorosulfonyl)imide (LiFSI) was purchased from KISHIDA CHEMICAL CO., Ltd. *N*-methyl-*N*-propylpyrrolidinium bis(fluorosulfonyl)imide ($Pyr_{13}FSI$) was purchased from KANTO CHEMICAL Co. LiFSI and $Pyr_{13}FSI$ were mixed at a molar ratio of 1:1. The water content of the prepared electrolytes was analyzed using the Karl Fischer titration method (Kyoto Electronic Manufacturing Co., Ltd., MKC-710). The water content was < 50 ppm.

2.2.3. Affinity test between the separator and electrolyte

The height of the electrolyte lifted by the capillary action of the separator is an indicator of its affinity for the electrolyte. A rectangular separator with a width of 1 cm was used as the sample. One end of each separator was immersed in the electrolyte for 1 h. Subsequently, the lifting heights of the electrolytes were measured.

2.2.4. Characterization of the Li metal anode and separator

The morphologies of the Li metal and separator were observed through scanning electron microscopy (SEM) (JSM-6490A, JEOL Ltd.). The cross-section of PI separator

was observed by Focused ion beam (FIB) coupled SEM (SMF2000, Hitachi High-Tech Corp.). The Ga ion beam for cross sectional cutting was accelerated by 30 kV. The cross section of PP separator was observed by plasma FIB-SEM (Helios 5, ThermoFischer Scientific Inc.). The N ion beam was used for cross sectional cutting. The acceleration voltage was 30 kV. The mechanical strength of each separator was measured using a tensile tester (Autograph AGS-X, SHIMADZU Corp.). The gas permeability of the separators was measured using a Gurley permeability tester (No. 158 GURLEY TYPE DENSOMETER; TOYOSEIKI Co., Ltd.). The chemical composition of the Li metal surface was analyzed through X-ray photoelectron spectroscopy (XPS, JPS-9010MX, JEOL Ltd.).

2.2.5. Ionic conductivity measurement

The ionic conductivity of the electrolyte in the separators was measured in the cells consisting of Au electrodes and an electrochemical measurement system (VMP-300, BioLogic Science Instruments). The impedance measurement was conducted using alternating current (AC) voltage with ±5 mV amplitude in the frequency ranges of 500 kHz to 100 mHz. The ionic conductivity, σ (S cm^{-1}), was determined using Equation (1) as follows:

$$\sigma = d/(R_b S), \quad (1)$$

where d denotes the separator thickness (cm), R_b is the bulk resistance (Ω), and S is the electrode area (cm^2). The measurement was conducted in the temperature range 15−50 °C to obtain Arrhenius plots of ionic conductivity. In general, the Arrhenius plot for ionic liquid is typically convex-shaped. Therefore, the curve fitting was conducted with the

Vogel-Tammann-Fulcher (VTF) equation including the effect of the glass transition temperature.[35–37] The VTF equation is expressed as follows:

$$\sigma = AT^{-1/2} \exp[-B/(T-T_0)], \quad (2)$$

where A is related to a pre-exponential factor (S cm^{-1} K$^{1/2}$), B is related to the activation energy (K), T is a temperature (K), and T_0 is the ideal glass transition temperature (K). [38–40]

2.2.6. Electrochemical measurements

Li/Li symmetric cells and $LiNi_{0.5}Mn_{0.2}Co_{0.3}O_2$ (NCM523)/Li full cells were constructed in a glovebox filled with Ar gas. Those cells used either a 3DOM PI separator or a surfactant-coated PP separator (Celgard®3401, Celgard, LCC) to evaluate the effect of the separator on Li deposition/dissolution behavior. Li foil on the Cu current collector (100 μm Li/10 μm Cu, Honjo Metal Co., Ltd.) was polished with a polystyrene brush and used in Li/Li symmetric cells. NCM523 electrode sheet (bcaf-ncm523ss, MTI Corp.) with 2 mAh cm^{-2} and polished Li foil on the Cu current collector (20 μm Li/10 μm Cu, Honjo Metal Co., Ltd.) were used in NCM523/Li full cells. All cells contained 50 μL of electrolyte. This excess amount of electrolyte is 600–850 % compared to the calculated from the porosity of separators and cathode.

The Li deposition/dissolution test of Li/Li symmetric cells and the charge/discharge test of NCM523/Li full cells were conducted at 30 °C using charge/discharge test equipment (TOSCAT-3100, TOYO SYSTEM Co., Ltd.). The Li deposition/dissolution test was performed at a capacity of 1 mAh cm^{-2}. The charge/discharge test of the NCM523/Li full cell was performed in the voltage range of

2.5–4.3 V with constant current-constant voltage mode for charging and constant current mode for discharging.

The cell impedances for Li/Li symmetric cells and NCM/Li full cells were measured using a frequency response analyzer built-in potentiostat/galvanostat (VMP-300, TOYO Corporation) with AC voltage with ±5 mV amplitude in the frequency ranges of 500 kHz to 100 mHz. The electrochemical impedance spectra were obtained at 30 °C.

2.3. Results and discussion

2.3.1. Properties of separators

Figures 2–1 (a) and (b) show the SEM images of the surfactant-coated PP and 3DOM PI separators. Pores 0.043 μm in size were non-uniformly distributed in the surfactant-coated PP separator.[20] Elongated pores in the same direction were observed at the cross-section of the separator because of the separator preparation process. In contrast, the 3DOM PI separator consisted of 300 nm macropores, which are regularly packed in a 3D space. In addition, approximately 75 nm pores connecting the pores between the macropores were also observed. The physical properties of the surfactant-coated PP and 3DOM PI separators are summarized in Table 1. The porosity of the surfactant-coated PP separator was 41 %, whereas that of the 3DOM PI separator was 78 %. The high porosity contributed to the uniform pore structure of the separator but resulted in a low mechanical strength of the 3DOM PI separator. The tensile strength of the surfactant-coated PP separator was 13 N, whereas that of the 3DOM PI separator was 1.5 N. The Gury numbers of the surfactant-coated PP and 3DOM PI separators were 620 and 160 s for 100 cm^3 of air, respectively. The 3DOM PI separator exhibited higher permeability owing to the large pore volume and their high connectivity. Figures 2–1 (e) and (f) show the lifting height

of the highly concentrated ILE by the capillary action of the surfactant-coated PP and 3DOM PI separators, respectively. The lifting height corresponded to the affinity of the electrolyte for the separator. A height of 1 mm was observed when the surfactant-coated PP separator was used, whereas a height of 5 mm was observed when the 3DOM PI separator was used. These results indicate that each separator has not only a different affinity for the electrolyte depending on the porosity and type of polymer material, but also different 3D pore structures.

The ionic conductivities of the surfactant-coated PP and 3DOM PI separators with highly concentrated ILE were investigated to study the effect of the separators on the ionic conductivity of the electrolyte. Figure 2–1 (g) shows the Arrhenius plots of the highly concentrated ILE in the separators. The intrinsic ionic conductivity of the bulk electrolyte at 30 °C was 1.40 mS cm^{-1}. The ionic conductivity of highly concentrated ILE in the surfactant-coated PP and 3DOM PI separators was 0.11 and 0.28 mS cm^{-1}, respectively. The ionic conductivities of the electrolyte in the surfactant-coated PP and 3DOM PI separators were lower than those in the bulk electrolyte. The ionic conductivity of the electrolyte with 3DOM PI separator was higher than that of the electrolyte with the surfactant-coated PP separator. The porosities and Gurley numbers of the separators were related to their ionic conductivities.[41,42] The porosity ratio between the surfactant-coated PP and 3DOM PI separators was 1:1.9 and the ionic conductivity ratio was 1:2.5. The ionic conductivity ratio expected from the porosity differed from the measured value. This difference may be attributed to the difference in the tortuosity of the separators or the interaction between the polymer matrix and highly concentrated ILE. The latter effect influences the activation energy of the ionic conductivity. The Arrhenius plots were fitted using the VTF equation (Equation (2)) to determine the parameter of *B*, which is related

to the activation energy for ion transport. The parameters of B for bulk electrolyte and those in the surfactant-coated PP and 3DOM PI separators were 897.0, 857.6, and 880.7 K, respectively. These values did not significantly differ from each other, indicating that the ion transport mechanisms of the bulk electrolyte and the electrolyte in separators were similar. Therefore, the interaction between the highly concentrated ILE and polymer matrix is almost negligible. In conclusion, the ionic conductivity of highly concentrated ILE in separators was determined by their tortuosity. The 3DOM structure exhibited smaller tortuosity, indicating that a uniform porous structure is suitable for achieving a lower resistance in real cells.

2.3.2. Li deposition/dissolution performance

Separators with different ionic conductivities exhibited different maximum current densities for stable Li deposition/dissolution reactions. Li deposition/dissolution tests were conducted using Li/Li symmetric cells at various current densities (0.1–3.0 mA cm^{-2}). The capacity of Li deposition/dissolution was 1.0 mAh cm^{-2}. Figures 2–2 (a) and (b) show the voltage profiles of the Li deposition/dissolution cycles at different current densities. For the cell with the surfactant-coated PP separator, the maximum current density was less than 2.0 mA cm^{-2}. In contrast, the stable voltage profile was observed at 3.0 mA cm^{-2} for the cell with the 3DOM PI separator. Stable Li deposition/dissolution cycles were realized because of the higher ionic conductivity and lower polarization.

The uniform current distribution leads to the improved performance of the Li deposition/dissolution cycle. The type of separator significantly influences the morphology of the Li metal deposits and the cycle life of the Li metal anodes. The cycle performance of Li metal was investigated using Li/Li symmetric cells with surfactant-

coated PP and 3DOM PI separators. The capacity for Li deposition/dissolution cycle was 1 mAh cm^{-2} and the current density was 1.0 mA cm^{-2}. Figures 2–2 (c) and (d) show the voltage profiles of the Li/Li symmetric cell with the surfactant-coated PP separator and the 3DOM PI separator. The cell with the surfactant-coated PP separator exhibited a polarization of 150 mV in the 1st cycle. The polarization then decreased to 110 mV over 60 cycles and rapidly decreased to 20 mV after the 80th cycle. In contrast, the cell with the 3DOM PI separator exhibited a stable polarization of approximately 50 mV for 50 cycles. Subsequently, the polarization gradually decreased to 20 mV.

Cell impedance is also important for investigating the stability of Li metal anodes. Figures 2–2 (e) and (f) show the Cole−Cole plots at the 1st, 2nd, 3rd, 10th, 50th, and 100th cycles. For the surfactant-coated PP separator, the interfacial resistance in the 1st cycle was six times higher than that before the first cycle. The bulk and interfacial resistances rapidly decreased from the 2nd to the 50th cycle because of the increase in the Li metal surface area. The bulk resistance at the 100th cycle increased, which was related to the decomposition and depletion of the electrolyte. Li metal, which has a large surface area, is highly reactive with the electrolyte, resulting in more active electrolyte decomposition. In contrast, the Li deposition/dissolution behavior of the 3DOM PI separator was more stable than that of the surfactant-coated PP separator over 100 cycles. The bulk and interfacial resistances of the cell with the 3DOM PI separator decreased gradually. After 100 cycles, the polarization of the 3DOM PI separator was similar to that of the surfactant-coated PP separator, this may be due to an increase in surface which leads to a decrease in SEI layer resistance. The uniform current distribution from the uniform porous structure of the 3DOM PI separator contributed to the uniform deposition of Li metal, resulting in better cycle performance of the Li metal anode than, that of the

cell with the surfactant-coated PP separator.

The morphology of the deposited Li metal was observed using SEM to investigate the effect of the 3DOM PI separator. The cell was disassembled after the 1st, 10th, and 50th cycles, and the Li metal surface was observed. Figures 2–3 (a–f) show SEM images of the deposited Li metal. The Li metal deposited in the cell with a surfactant-coated PP separator was not uniform. Whisker-like deposits were observed even in the 1st and 10th cycles. In the 50th cycle, large and significantly fine particles were observed, which actively reacted with the electrolytes. In contrast, the Li metal deposited in the cell with the 3DOM PI separator, after all cycles, exhibited a granular size of 10 μm. The surface area of Li metal was smaller and it suppressed chemical reactions with the electrolyte. These results are consistent with the behavior of the Cole–Cole plots.

The composition of the SEI layer is considered one of the important parameters required for a stable Li deposition/dissolution reaction.[43–47] During the deposition of Li metal, the electrolyte decomposes to form SEI layers. The SEI layers of the deposited Li metal in the 1st cycle of the cells with the surfactant-coated PP and 3DOM PI separators were analyzed through XPS. Figure 2–4 shows F1s, O1s, and C1s spectra. The peak positions and intensities were not significantly different. The compositions of the SEI layers of the surfactant-coated PP and 3DOM PI separators were similar. Therefore, the difference in Li deposition/dissolution performance is attributed to the ionic conductivity and morphology of the deposited Li metal. The significant internal resistance observed in the 1st cycle of the cell with the surfactant-coated PP separator may be attributed to the severe decomposition behavior of ILE or non-uniform volume expansion of the Li metal owing to the concentrated current distribution. In contrast, the surface area of the Li metal

deposited with the 3DOM PI separator was smaller, which suppressed the chemical reaction. From these results, it is evident that the 3DOM PI separator with a uniform porous structure provides a more uniform deposition of Li metal and more reversible deposition/dissolution cycle behavior than other separators with non-uniform porous structures.

2.3.3. NCM523/Li full cell performance

The performance of the separators was investigated using NCM523/Li full cells with Li metal anodes and cathodes. NCM523/Li full cells with surfactant-coated PP or 3DOM PI separator were also prepared. Charge/discharge tests were conducted on both full cell types. Figure 2–5 (a) shows discharge capacities at various currents in the range of 0.1–1.0 C rate (0.2–2.0 mA cm^{-2}). The discharge capacity of the cell with the surfactant-coated PP and 3DOM PI separators were 164.6 and 172.1 mAh g^{-1} at 0.1 C rate, and 15.8 and 117.5 mAh g^{-1} at 1.0 C rate, respectively. The charge/discharge test was conducted at 0.1 C rate after the rate capability test, and the discharge capacities of both cells recovered. The 3DOM PI separator exhibited a higher rate capability than the surfactant-coated PP separator. These results indicate that the ionic conductivity of highly concentrated ILE in the separators significantly affects their rate capabilities.

Figure 2–5 (b) shows the discharge capacity and coulombic efficiency over 50 cycles. The charge/discharge test was conducted at 0.1 C rate for the initial three cycles and at 0.5 C rate after the 4th cycle. The discharge capacity of the cell with the surfactant-coated PP separator was 130.0 mAh g^{-1} at the 4th cycle. Thereafter it gradually decreased to 45.8 mAh g^{-1} at the 50th cycle. In the case of the 3DOM PI separator, the discharge capacity was 160.6 mAh g^{-1} at the 4th cycle, which was maintained during 50 cycles. The

charge/discharge curves are shown in Figs. 2–6 (a) and (b). The polarization of the cell with the surfactant-coated PP separator increased during the cycling tests. The charge/discharge curves of the cell with the 3DOM PI separator did not change significantly, indicating that the internal resistance was stable during cycling. The coulombic efficiency of the cell with the surfactant-coated PP separator was 83.79 % in the initial cycle, whereas the average coulombic efficiency from the 5th cycle to the 50th cycle was 97.56 %. For the 3DOM PI separator, the coulombic efficiency was 88.71 % in the initial cycle, whereas the average coulombic efficiency from the 5th cycle to the 50th cycle was 99.89 %. The 3DOM PI separator contributed to a more stable discharge capacity and higher coulombic efficiency than the surfactant-coated PP separator.

Cell impedance during the charge/discharge process was investigated to evaluate the stability of the NCM523/Li full cells. EIS was performed at a state of charge of 10 %. Figures 2–5 (c) and (d) show the Cole–Cole plots. The interfacial resistance of the cell with the surfactant-coated PP separator increased during the 2nd and 3rd cycles. This behavior may be due to the severe decomposition behavior of ILE or the non-uniform volume expansion of the Li metal anode and cathode owing to the concentrated current distribution. The bulk resistance increased after the 10th cycle. This may be related to electrolyte depletion. This behavior was also supported by the low coulombic efficiency in the charge/discharge cycles. For the 3DOM PI separator, the bulk and interfacial resistances decreased from the 3rd cycle to the 10th cycle owing to the increase in the Li metal surface area. Subsequently, the Cole–Cole plot exhibited stable behavior over 40 cycles.

The morphology of the deposited Li metal was observed through SEM to investigate the effect of the 3DOM PI separator on the NCM523/Li full cell. The cell was

deconstructed after the 1st, 10th, and 50th cycles, and the Li metal surface was observed. Figures 2–6 (a–f) show SEM images of the deposited Li metal. The Li metal deposited in the full cell with the surfactant-coated PP separator after all cycles was whisker-like with a high surface area. In contrast, the deposited Li metal in the full cell with the 3DOM PI separator, after all cycles, exhibited a granular size of 10 μm.

These results are consistent with each other. The uniform electrode reaction provided by the 3DOM PI separator reduces the surface area of the Li metal and thus suppresses excessive electrolyte decomposition. The suppression of side reactions results in a more reversible charge/discharge reaction and higher coulombic efficiency. This behavior provided a lower internal resistance and high discharge capacity over 50 cycles.

2.4. Conclusion

In this study, a 3DOM PI separator was proposed as a high-affinity separator for highly concentrated ILE. Both the affinity for ILE and the electrochemical properties of the 3DOM PI separator were investigated and compared with those of conventional surfactant-coated PP separators. The 3DOM PI separator comprised polyimide and exhibited high porosity and a 3D-ordered pore structure. These properties provided a better affinity for highly concentrated ILE and higher ionic conductivity than those of the surfactant-coated PP separator. The higher ionic conductivity of the 3DOM PI separator with ILE provided a higher maximum current density of Li metal deposition/dissolution for Li/Li symmetric cells and a higher rate capability for the NCM523/Li full cell. These observations indicate that the ionic conductivity of highly concentrated ILE in the separators significantly affects their rate capabilities. Moreover, the Li/Li symmetric cell and NCM523/Li full cell with the 3DOM PI separator provided more stable internal

resistance and cycle performance than those with the surfactant-coated PP separator. Because the chemical composition of the SEI layer on the Li metal surface was almost the same, the morphology of the deposited Li metal was an important factor determining the cycle performance of the cells. The 3D-ordered uniform pore structure of the 3DOM PI separator provided a non-dendritic Li metal deposition morphology, resulting in high coulombic efficiency and high cycle stability.

Table 1. Physical properties of the surfactant-coated PP and the 3DOM PI separator.

	Tickness [µm]	Pore size [nm]	Porosity [%]	Tensile strength [N]	Gurley number [s cm^{-3}]
Surfactant-caoted PP	25	43	41	13	620
3DOM PI	28	300 (75)	75	1.5	160

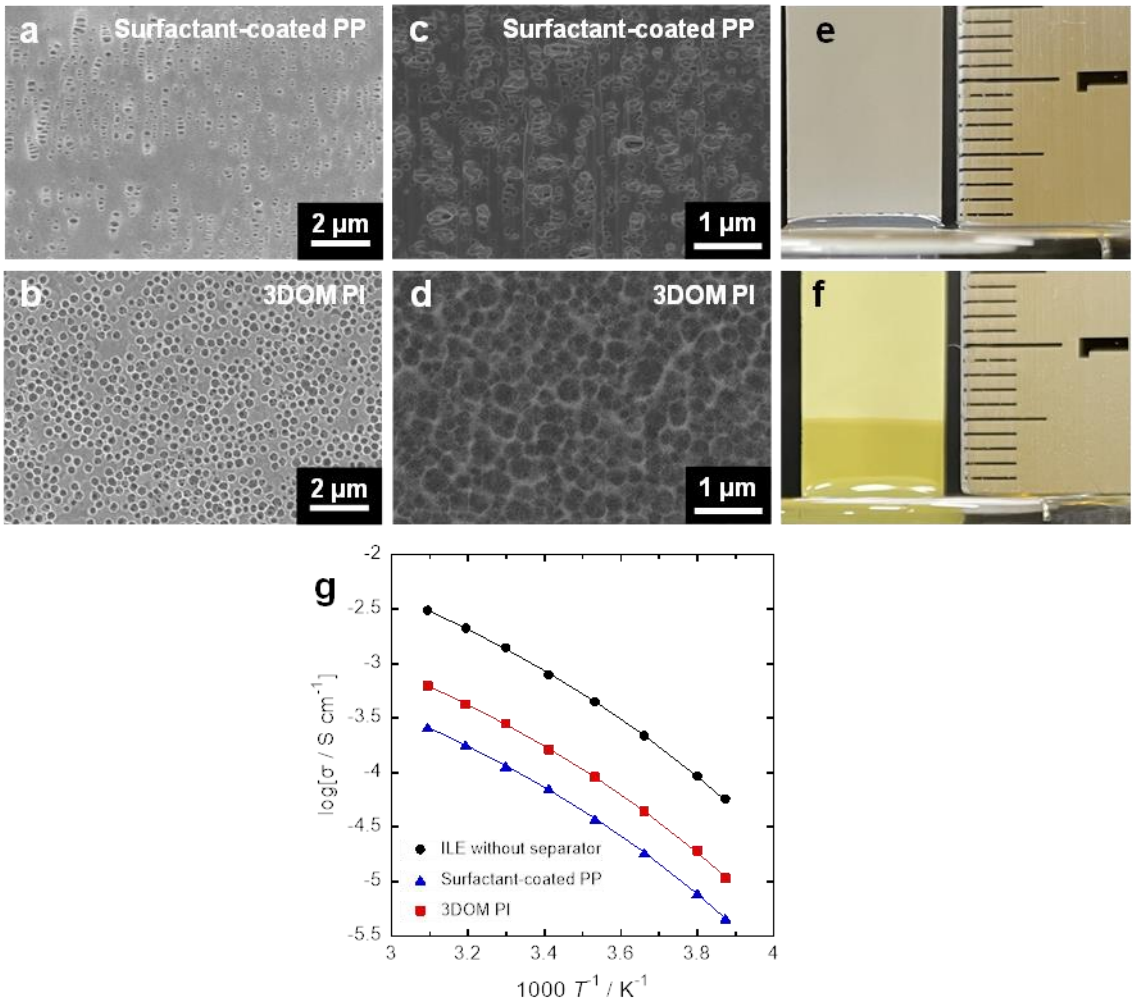

Figure 2–1. SEM images of surfactant-coated PP and 3DOM PI separators; (a) surface of the surfactant-coated PP separator, (b) surface of the 3DOM PI separator, (c) cross section of the surfactant-coated PP separator, and (d) cross section of the 3DOM PI separator. Lift up of ILE by (e) surfactant-coated PP separator and (f) 3DOM PI separator. (g) Arrhenius plots of ionic conductivities of various separators including ILE.

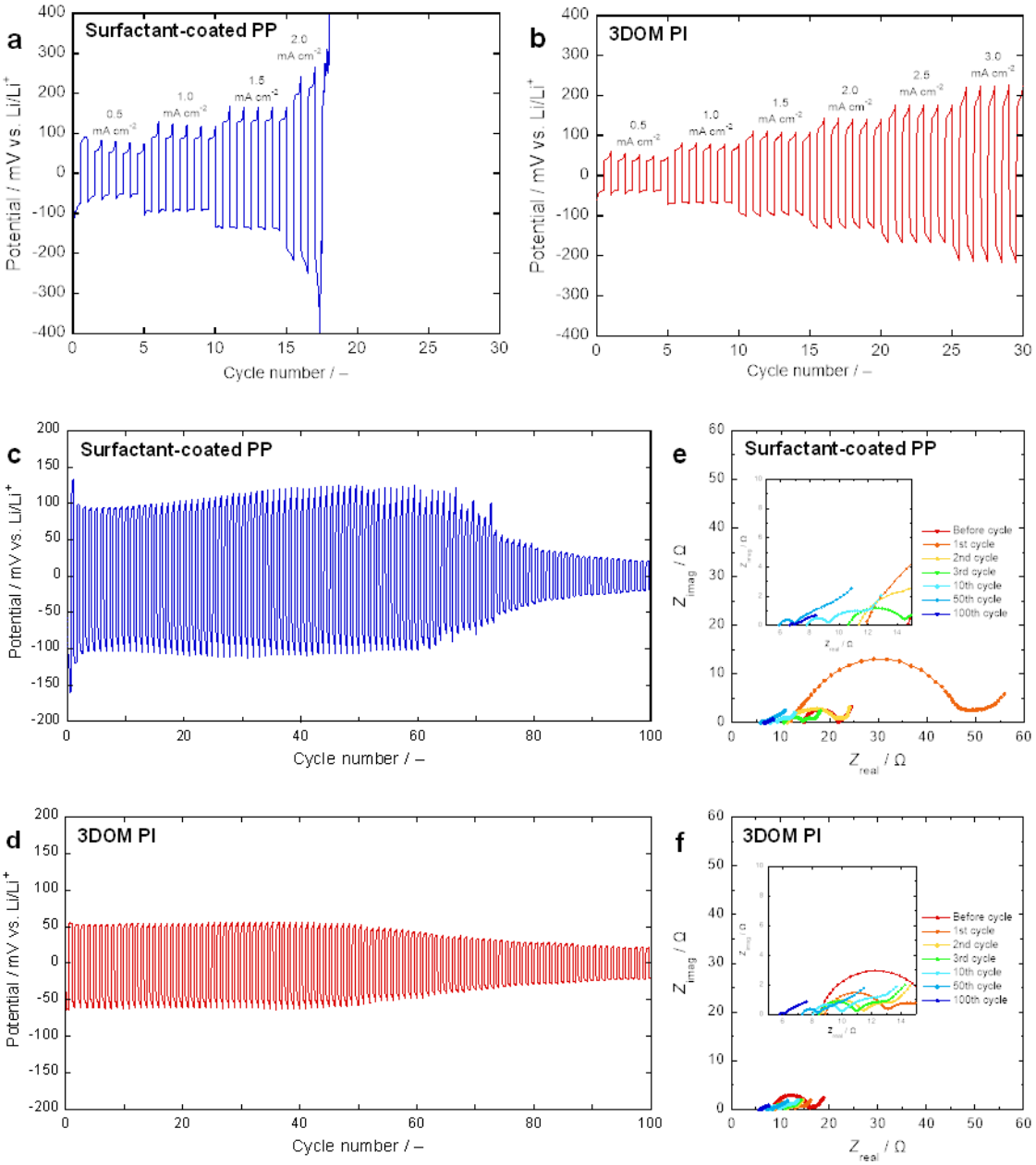

Figure 2–2. Voltage profiles of Li/Li symmetrical cells at various current densities using (a) surfactant-coated PP separator and (b) 3DOM PI separator. Voltage profiles of Li/Li symmetrical cells at 1.0 mA cm^{-2} using (c) surfactant-coated PP separator and (d) 3DOM PI separator. Cole–Cole plots during Li deposition/dissolution cycles in Li/Li symmetrical cells using (e) surfactant-coated PP separator and (f) 3DOM PI separator.

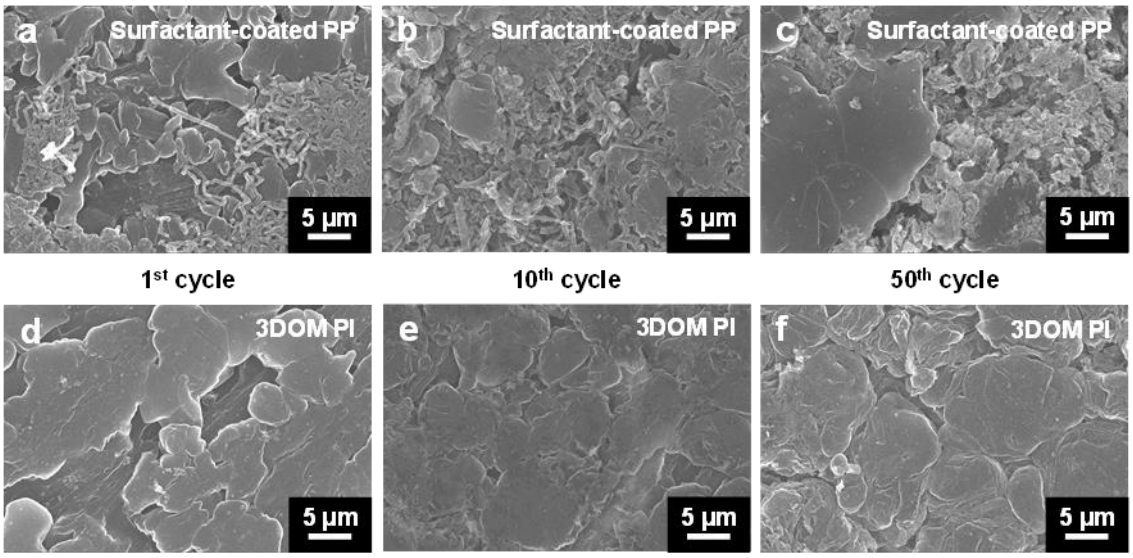

Figure 2–3. SEM images of deposited Li metal surface in Li/Li symmetrical cells using (a–c) surfactant-coated PP separator and (d–f) 3DOM PI separator after different charge/discharge cycles.

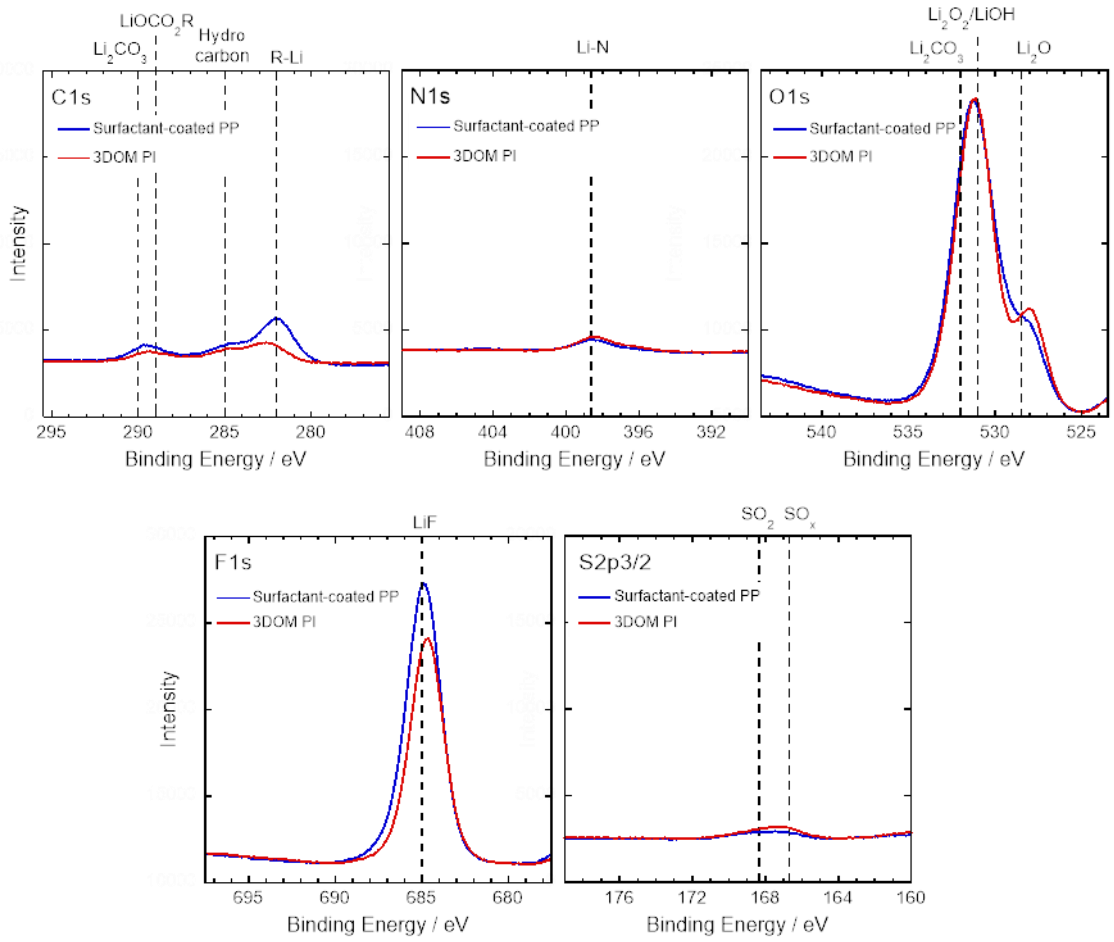

Figure 2–4. C1s, N1s, O1s, F1s, and S XPS spectra of the SEI layer on deposited Li metal at the initial cycle in Li/Li symmetrical cells (blue line: surfactant-coated PP separator and red line: 3DOM PI separator).

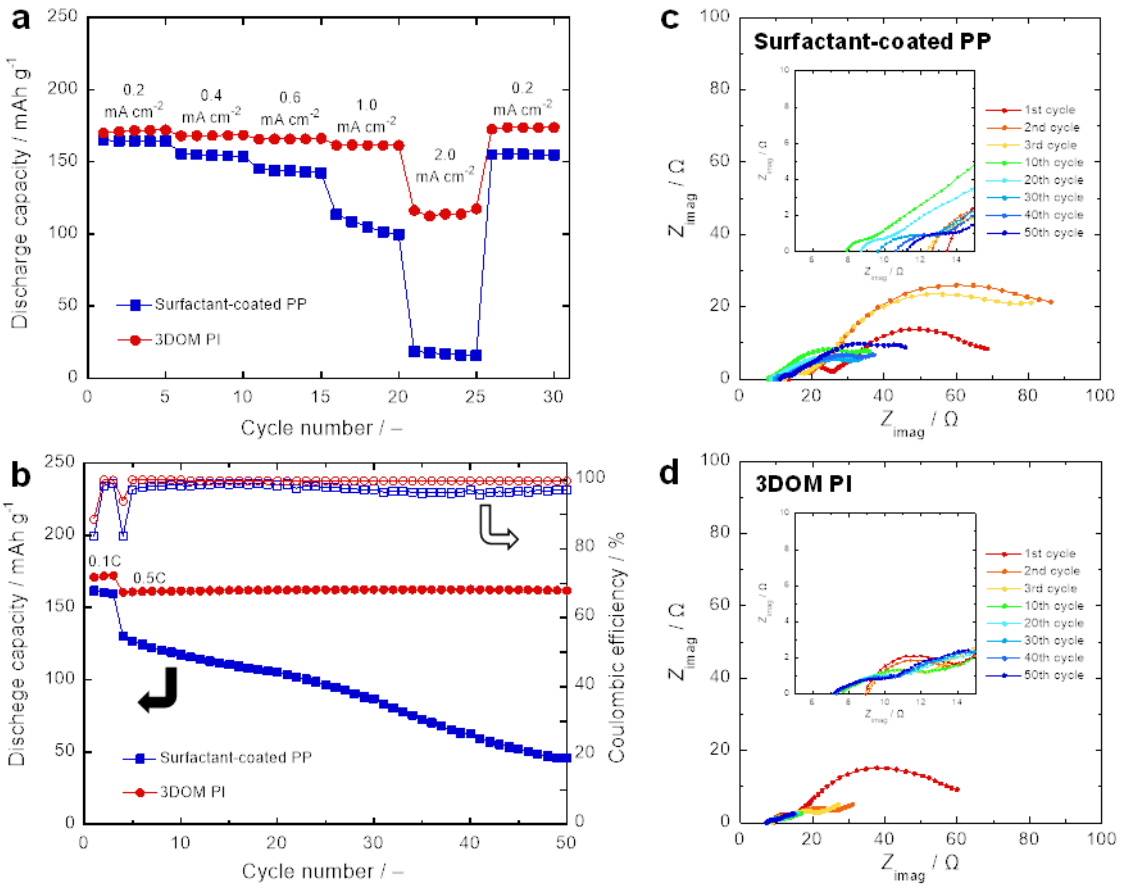

Figure 2–5. (a) Discharge capacity of NCM523/Li full cells at various current densities. (b) Discharge capacity and coulombic efficiency of NCM523/Li full cells. Cole–Cole plots during charge-discharge cycles in NCM523/Li full cells using (c) surfactant-coated PP separator and (d) 3DOM PI separator.

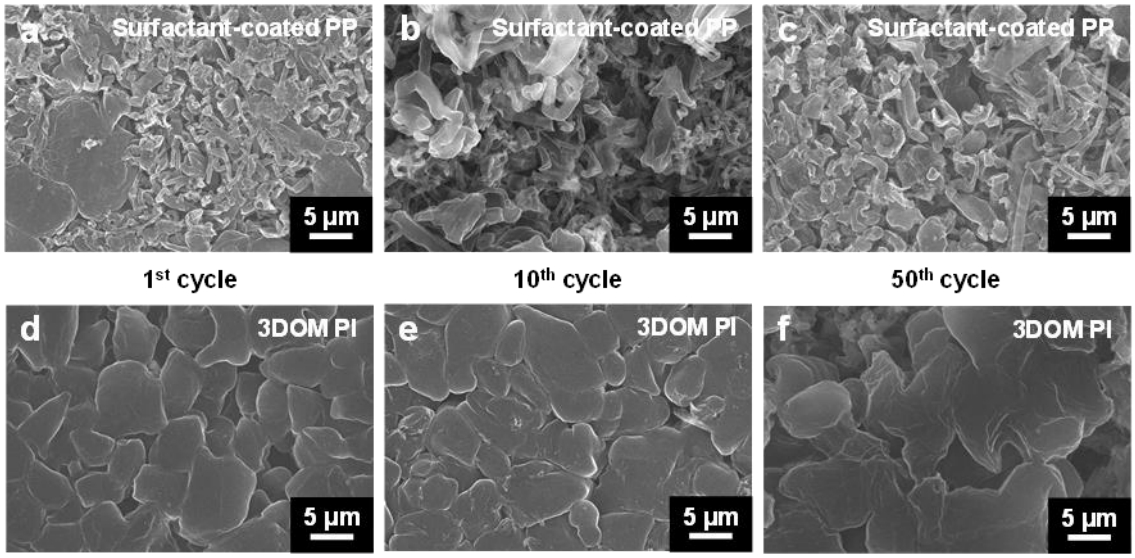

Figure 2–6. SEM images of deposited Li metal surface in NCM523/Li full cells using (a–c) surfactant-coated PP separator and (d–f) 3DOM PI separator.

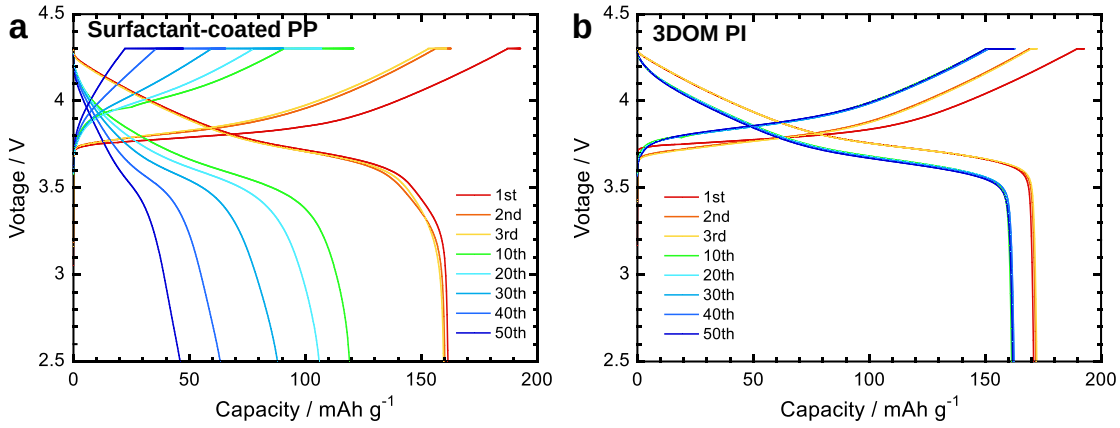

Figure 2–6. Charge/discharge curves of the NCM523/Li full cell with (a) surfactant-coated PP separator and (b) 3DOM PI separator.

2.5. References

1. J. M. Tarascon and M. Armand, Nature, 414, 359 (2001).
2. D. Aurbach, A. Zaban, A. Schechter, Y. Eineli, E. Zinigrad, and B. Markovsky, J. Electrochem. Soc., 142, 2873 (1995).
3. K. Xu, Chem. Rev., 104, 4303 (2004).
4. W. Xu, J. L. Wang, F. Ding, X. L. Chen, E. Nasybutin, Y. H. Zhang, and J. G. Zhang, Energy Environ. Sci., 7, 513 (2014).
5. D. P. Lu, Y. Y. Shao, T. Lozano, W. D. Bennett, G. L. Graff, B. Polzin, J. G. Zhang, M. H. Engelhard, N. T. Saenz, W. A. Henderson, P. Bhattacharya, J. Liu, and J. Xiao, Adv. Energy Mater., 5 (2015).
6. Y. S. Fung and R. Q. Zhou, J. Power Sources, 81, 891 (1999).
7. H. Sakaebe and H. Matsumoto, Electrochem. Commun., 5, 594 (2003).
8. P. C. Howlett, D. R. MacFarlane, and A. F. Hollenkamp, Electrochem. Solid-State Lett., 7, A97 (2004).
9. H. Matsumoto, H. Sakaebe, K. Tatsumi, M. Kikuta, E. Ishiko, and M. Kono, J. Power Sources, 160, 1308 (2006).
10. T. Evans, J. H. Lee, V. Bhat, and S. H. Lee, J. Power Sources, 292, 1 (2015).
11. Q. W. Huang, Y. Y. Lee, and B. Gurkan, Ind. Eng. Chem. Res., 58, 22587 (2019).
12. G. B. Appetecchi, M. Montanino, M. Carewska, M. Moreno, F. Alessandrini, and S. Passerini, Electrochim. Acta, 56, 1300 (2011).
13. H. Yoon, P. C. Howlett, A. S. Best, M. Forsyth, and D. R. MacFarlane, J. Electrochem. Soc., 160, A1629 (2013).

14. G. M. A. Girard, M. Hilder, H. Zhu, D. Nucciarone, K. Whitbread, S. Zavorine, M. Moser, M. Forsyth, D. R. MacFarlane, and P. C. Howlett, Phys. Chem. Chem. Phys., 17, 8706 (2015).

15. R. Furuya, T. Hara, T. Fukunaga, K. Kawakami, N. Serizawa, and Y. Katayama, J. Electrochem. Soc., 168 (2021).

16. P. Arora and Z. M. Zhang, Chem. Rev., 104, 4419 (2004).

17. S. S. Zhang, J. Power Sources, 164, 351 (2007).

18. X. S. Huang, J. Solid State Electrochem., 15, 649 (2011).

19. H. Lee, M. Yanilmaz, O. Toprakci, K. Fu, and X. W. Zhang, Energy Environ. Sci., 7, 3857 (2014).

20. M. Eftekharnia, M. Hasanpoor, M. Forsyth, R. Kerr, and P. C. Howlett, ACS Appl. Energy Mater., 2, 6655 (2019).

21. H. Munakata, D. Yamamoto, and K. Kanamura, Chem. Commun., 3986 (2005).

22. K. Kanamura, T. Mitsui, and H. Munakata, Chem. Mater., 17, 4845 (2005).

23. D. Yamamoto, H. Munakata, and K. Kanamura, J. Electrochem. Soc., 155, B303 (2008).

24. H. Munakata, D. Yamamoto, and K. Kanamura, J. Power Sources, 178, 596 (2008).

25. Y. Maeyoshi, D. Ding, M. Kubota, H. Ueda, K. Abe, K. Kanamura, and H. Abe, ACS Appl. Mater. Interfaces, 11, 25833 (2019).

26. D. Kim, H. Munakata, J. Park, Y. Roh, D. Jin, M. H. Ryou, K. Kanamura, and Y. M. Lee, ACS Appl. Energy Mater., 3, 3721 (2020).

27. K. Takemoto, J. Wakasugi, Y. Maeyoshi, H. Michibata, T. Matsushita, M. Kubota, H. Abe, and K. Kanamura, J. Power Sources, 478 (2020).

28. K. Takemoto, J. Wakasugi, M. Kubota, H. Abe, and K. kanamura, Electrochemistry, 89, 197 (2021).

29. X. B. Cheng, R. Zhang, C. Z. Zhao, F. Wei, J. G. Zhang, and Q. Zhang, Adv. Sci., 3, 1500213 (2016).

30. Y. Maeyoshi, S. Miyamoto, H. Munakata, and K. Kanamura, J. Power Sources, 350, 103 (2017).

31. Y. Shimizu and K. Kanamura, J. Electrochem. Soc., 166, A754 (2019).

32. M. Nagasaki and K. Kanamura, ACS Appl. Energy Mater., 2, 3896 (2019).

33. J. Takeyoshi, N. Kobori, and K. Kanamura, Electrochemistry, 88, 540 (2020).

34. R. Miyagawa, J. Takeyoshi, K. Kanamura, S. Taminato, D. Mori, and N. Imanishi, Electrochemistry, 90 (2022).

35. C. A. Angell, J. Phys. Chem., 68, 1917 (1964).

36. A. Noda, K. Hayamizu, and M. Watanabe, J. Phys. Chem. B, 105, 4603 (2001).

37. W. Xu, E. I. Cooper, and C. A. Angell, J. Phys. Chem. B, 107, 6170 (2003).

38. H. Vogel, Phys. Z., 22, 645 (1921).

39. G. S. Fulcher, J. Am. Ceram. Soc., 75, 1043 (1992).

40. G. Tammann and W. Hesse, Z. Anorg. Allg. Chem., 156, 245 (1926).

41. J. Jang, J. Oh, H. Jeong, W. Kang, and C. Jo, Materials, 13 (2020).

42. C. F. J. Francis, I. L. Kyratzis, and A. S. Best, Adv. Mater., 32 (2020).

43. X. Wang, W. Zeng, L. Hong, W. W. Xu, H. K. Yang, F. Wang, H. G. Duan, M. Tang, and H. Q. Jiang, Nat. Energy, 3, 227 (2018).

44. F. Hao, A. Verma, and P. P. Mukherjee, J. Mater. Chem. A, 6, 19664 (2018).

45. M. Ue and K. Uosaki, Curr. Opin. Electrochem., 17, 106 (2019).

46. H. P. Wu, H. Jia, C. M. Wang, J. G. Zhang, and W. Xu, Adv. Energy Mater., 11 (2021).

47. S. Park, R. Chaudhary, S. A. Han, H. Qutaish, J. Moon, M. S. Park, and J. H. Kim, Energy Mater., 3 (2023).

Chapter 3: Improvement of the Electrochemical Performances of Li-Metal Anode by Composite of Ion Gel Electrolyte and Three-Dimensionally Ordered Macroporous Polyimide Separator

3.1. Introduction

Li-metal anode is one of the most promising anode materials because of its high theoretical capacity (3860 mAh g^{-1}) and extremely low redox potential (–3.04 V vs. SHE). [1,2] Li-metal anode has been combined with various cathode materials to fabricate next-generation rechargeable batteries, such as Li-air, Li-S, and Li-metal batteries (LMBs). [3,4] However, Li-metal anode has various problems, such as low cycle performance caused by an internal short circuit owing to nonuniform Li deposition during cycling and low coulombic efficiency owing to a breakdown of a solid electrolyte interface (SEI) layer by a volume change of Li metal. [5,6] In addition, some carbonate-based electrolytes used in LMBs are highly flammable and volatile, leading to serious problems in the safety of LMBs. [7] To keep the safety of LMBs, the operating temperature of LMBs is limited to around room temperature. Moreover, an introduction of cooling systems is sometimes required, resulting in a reduction of energy density. Therefore, the electrolyte used in LMBs should contribute to high cycle performances, coulombic efficiency, and safety.

Some electrolytes have been incorporated into polymer matrices, such as poly(ethylene oxide) (PEO), poly(vinylidene fluoride-co-hexafluoropropylene) (PVDF-HFP), and poly(methyl methacrylate) (PMMA), to form gel polymer electrolytes (GPEs) to realize higher safety of electrolytes. [8-13] These electrolytes having a low volatility

improve the safety of LMBs. Particularly, GPEs can suppress a leakage of electrolytes contributing a higher battery safety and an easier fabrication of battery. [14] On the other hand, ionic liquid electrolytes (ILEs) have attracted much attention as a candidate for electrolytes with high safety. [15,16] ILs are salts in the liquid state consisting only of anions and cations, with negligible volatility and high thermal stability. Various combinations of anions and cations have been investigated as ILEs for LMBs. Pyrrolidinium-based ILEs have been reported as the most promising electrolyte with higher electrochemical stability and ionic conductivity. [17-20] It has been reported that highly concentrated LIEs with high Li salt concentration have improved Li^+ transferase number, rate performances, and cycle performances owing to a unique lithium conduction mechanism[21,22].

GPE with ILEs has attracted attention as a safe electrolyte, which was reported in 1993. [23] Watanabe et al. have developed the GPEs with ILs, which are so-called "ion gels" (IGs). [24] An amount of polymer matrix is minimized to achieve high ionic conductivity of IGs. However, the mechanical strength of the IGs is decreased with decreasing amount of polymer. The high mechanical strength is required to prepare the self-standing thin membrane of IGs. So far, various investigations have been conducted to resolve the trade-off relationship between ionic conductivity and mechanical strength of IGs. [14] Recently, various polymer matrices for IGs have been developed, such as functional polyhedral oligomeric silsesquioxane (POSS)-crosslinked poly(ethylene glycol) (PEG) hybrid networks and tetra-arm poly(ethylene glycol) (TetraPEG) with higher mechanical strength. [25,26] Thinner (<30 μm) electrolytes are required to improve the energy density of LMBs. To prepare a thin IG electrolyte, a composite between IG electrolytes and a poly-olefin separator has been proposed. [26] In the report, the demonstration for the charge–discharge of cells has been conducted by using composite

electrolytes between IG electrolytes and a surfactant-coated polypropylene (PP) separator.

In the case of a high-area capacity cycle for cells with Li metal anode, the separator strongly affects the cycle performance of the cell. [19,27] We have developed an ultrafine porous polyimide membrane with an inverse opal structure. This membrane is a three-dimensionally ordered microporous polyimide (3DOM PI). [28-30] The uniform structure of this separator is very useful for achieving uniform Li^+ flux and improving a cycle performance of Li-metal anodes. Another very important aspect of the 3DOM PI separator is its high affinity to highly viscous electrolytes, such as concentrated electrolytes and ILEs, which have not been utilized in lithium batteries. [31,32] This separator enables to use of these electrolytes in Li batteries with carbon or Li-metal anode. The combination of the 3DOM PI and highly viscous electrolytes provides a better cycle performance for Li-metal anodes.

In this report, we propose a 3DOM PI–IG composite electrolyte employing pyrrolidinium-based highly concentrated ILE, which is a quasi-solid electrolyte. PMMA was used as a polymer matrix of IG electrolytes. By using the separators as a framework of composite electrolytes, a self-standing membrane with less than 30 μm thickness was successfully prepared by using IG electrolytes with low mechanical strength. The three types of electrolytes were compared here: IG electrolyte, PP–IG composite electrolyte, and 3DOM PI–IG composite electrolyte. The unique structure of the 3DOM PI separator also achieves higher ionic conductivity and a highly reversible Li deposition/dissolution cycle, compared with the other electrolytes. Full cells with a $LiNi_{0.5}Co_{0.2}Mn_{0.3}O_2$ (NCM523, 2.0 mAh cm^{-2}) cathode and Li-metal anode were also fabricated by employing the 3DOM PI–IGE composite electrolyte. The better charge-discharge cycle performances were confirmed.

3.2. Experimental

3.2.1. Preparation process of 3DOM PI–IG composite electrolyte

An IG electrolyte precursor was cast on the surfactant-coated PP or 3DOM PI separator and sandwiched between a polytetrafluoroethylene (PTFE) sheet and then heated at 75 °C for 12 hours for in-situ polymerization in the separator. In the case of pristine IG electrolyte, the thickness of the self-standing membrane was controlled by 300 μm spacers. The preparation procedure of the 3DOM PI separator has been reported previously. IG electrolyte precursor was prepared from the highly concentrated ILE and polymeric precursor solution with mixing weight ratio of 90:10. The highly concentrated ILE was prepared from Li bis(fluorosulfonyl)imide (LiFSI, KISHIDA CHEMICAL CO., Ltd.) and *N*-methyl-*N*-propylpyrrolidinium bis(fluorosulfonyl)imide ($Pyr_{13}FSI$, KANTO CHEMICAL Co., Inc,). LiFSI and $Pyr_{13}FSI$ were mixed in a molar ratio of 1:1. The water content of the preparation electrolyte was confirmed to be lower than 50 ppm, using the Karl Fischer titration method (Kyoto Electronic Manufacturing Co., Ltd., MKC-710). Polymeric precursor solution was prepared from methyl methacrylate (MMA, FUJIFILM Wako Pure Chemical Corp.), 5 wt% of ethylene glycol dimethacrylate (EDGMA, FUJIFILM Wako Pure Chemical Corp.) to MMA, and 0.2 wt.% of 2,2'-azobis(isobutyronitrile) (AIBN, FUJIFILM Wako Pure Chemical Corp.) to MMA.

3.2.2. Physical characterization of the composite electrolyte and Li-metal anode

The morphologies of the separators and Li metal were observed using scanning electron microscopy (SEM) (JSM-6490A, JEOL Ltd.). The gas permeability of the separators was measured by using a Gurley permeabilities tester (No. 158 GURLEY

TYPE DENSOMETER, TOYOSEIKI Co., Ltd.). The mechanical strength of the separators and composite electrolytes was measured by using a tensile tester (Autograph AGS-X, SHIMADZU Corp).

3.2.3. Electrochemical characterization of the electrolytes

The cationic transference numbers t_+ of the electrolytes were measured using a frequency response analyzer built-in potentiostat/galvanostat (VMP-300, BioLogic Science Instruments) and Equation (1) as follows:

$$t_+ = i_s(\Delta V - i_0 R_0) / i_0(\Delta V - i_s R_s) \quad (1)$$

where ΔV is the applied voltage (V), i is the current (A), and R is the interfacial resistance (Ω). Subscripts 0 and s indicate the initial and steady-state values, respectively. [33-36] Here, the ΔV was 5 mV, and the impedance measurement was performed using alternating current (AC) voltage with ±5 mV amplitude in the frequency ranges from 500 kHz to 50 mHz.

The ionic conductivity of the electrolytes was measured also using pouch-type cells with two Au electrodes and a frequency response analyzer built-in potentiostat/galvanostat (VMP-300). The impedance measurement was performed using AC voltage with ±5 mV amplitude in the frequency ranges of 500 kHz to 50 mHz. The ionic conductivity, σ (S cm^{-1}), was determined using Equation (2) as follows:

$$\sigma = d/(R_b S) \quad (2)$$

where d denotes the separator thickness (cm), R_b is the bulk resistance (Ω), and S is the electrode area (cm^2). The ionic conductivity measurement was performed in the temperature range of 15–50 °C. In general, the Arrhenius plot for ILs and IGs is typically convex-shaped. Therefore, the curve was fitted with the Vogel-Tammann-Fulcher (VTF)

equation including the effect of the glass transition temperature. [37-39] The VTF equation is expressed as Equation (3) as follows:

$$\sigma = AT^{-1/2} \exp[-B/(T-T_0)] \quad (3)$$

where A is related to a pre-exponential factor (S cm^{-1} K$^{1/2}$), B is related to the activation energy (K), T is a temperature (K), and T_0 is the ideal glass transition temperature (K) [40-42].

3.2.4. Li deposition/dissolution tests

The Li/Cu pouch-type cells were constructed by using the prepared electrolytes, Li metal on the Cu current collector (100 μm Li/10 μm Cu, Honjo Metal Co., Ltd.), and Cu current collector. The cells were fabricated in an Ar-filled glovebox. Three types of electrolytes were used: pristine IG electrolyte, PP–IG composite electrolyte, and 3DOM PI–IG composite electrolyte. Li deposition/dissolution tests were performed at a current density of 0.25 mA cm^{-2} for 1 hour at 30 °C using charge–discharge test equipment (TOSCAT-3100, TOYO SYSTEM Co., Ltd.). The cut-off voltage of the dissolution process was set at 2.5 V. The cell impedances for Li/Cu cells were measured using a frequency response analyzer built-in potentiostat/galvanostat (VMP-300) with AC voltage with ±5 mV amplitude in the frequency ranges from 500 kHz to 50 mHz.

3.2.5. Charge–discharge test of the full cells

The pouch-type full cells were constructed by using the electrolytes, NCM523 (bcaf-ncm523ss, MTI Corp.) with 2 mAh cm^{-2}, and Li metal on the Cu current collector (20 μm Li/10 μm Cu, Honjo Metal Co., Ltd.) in an Ar-filled glovebox. Three types of electrolytes were used: pristine IG electrolyte, PP–IG composite electrolyte, and 3DOM

PI–IG composite electrolyte. The charge/discharge test of NCM523/Li full cells was performed at 30 °C using charge/discharge test equipment (TOSCAT-310). The charge/discharge test of the NCM523/Li full cell was performed with a constant current-constant voltage (CC-CV) mode for charging and a CC mode for discharging in the voltage range of 2.5–4.3 V.

3.3. Results and discussion

3.3.1. Physical properties of the electrolytes

Figures 3–1 (a–c) show photographs of the prepared electrolytes: pristine IG electrolyte, PP–IG composite electrolyte, and 3DOM PI –IG composite electrolyte. These electrolytes were prepared as self-standing membranes with thicknesses of 300, 25, and 30 μm, respectively. Figures 3–1 (d) and (e) show the SEM images of the surface and Figs. 3–1 (e) and (f) show the SEM images of the cross-section for surfactant-coated PP and 3DOM PI separators. The surfactant-coated PP separator consisted of nonuniformly distributed pores with less than 50 nm size, while the 3DOM PI separator consisted of uniformly distributed pores with approximately 300 nm size. The connecting pores with approximately 75 nm size were also observed in the 3DOM PI separator. Figures 3–1 (g) and (h) show the cross-sectional SEM images of PP–IG and 3DOM PI–IG composite electrolytes. The original porous structure of the pristine separators was confirmed from the cross-sectional SEM images. In contrast, no open pores were observed in the composite electrolyte, indicating that all pores were filled with the IG electrolyte. The porosity and Gurley number of the separators are listed in Table 1. The porosity of the surfactant-coated PP separator was 41 %, while that of the 3DOM PI separator was 78 %. The higher porosity corresponded to the uniform pore structure of the separator. The

Gurley number of the surfactant-coated PP and 3DOM PI were 620 and 160 sec for 100 cm^3 of air, respectively. The higher permeability of the 3DOM PI separator is due to the higher porosity and connectivity of pores.

A tensile strength test was performed to investigate the mechanical strength of the prepared electrolytes. Figures 3–2 (a) and (b) show the stress–strain curves of the pristine electrolytes and the prepared composite electrolytes. The tensile strength of the pristine IG electrolyte, PP–IG composite electrolyte, and 3DOM PI–IG composite electrolyte were 0.05, 13.23, and 0.80 N, respectively. The pristine IG electrolyte exhibited extremely low mechanical strength, but the mechanical strength of the composite electrolytes was significantly improved by the separators as a framework. The mechanical strength of the surfactant-coated PP and 3DOM PI separators was 13.12 and 0.96 N, respectively, which were comparable to those of the composite electrolytes. These results indicate that the mechanical strength of the composite electrolytes depends on those of separators as a framework. The lower porosity of the surfactant-coated PP electrolyte may contribute to higher mechanical strength.

3.3.2. Electrochemical properties of the electrolytes

An ionic conductivity measurement was performed to investigate the effect of the separators on the ionic conductivities. Figure 3–3 (a) shows the Arrhenius plots of the ionic conductivity of the electrolytes. The ionic conductivity of pristine IG electrolyte, PP–IG composite electrolyte, and 3DOM–IG composite electrolyte were 0.61, 0.06, and 0.16 mS cm^{-1}, respectively. The pristine IG electrolyte exhibited the highest ionic conductivity, followed by 3DOM–IG and PP–IG composite electrolytes. There was no significant difference in the slope of Arrhenius plots, indicating that the ionic conduction

mechanisms of these electrolytes were similar to each other. Therefore, the interaction between the separator and IG electrolyte is negligible. Since the pore structure of the separator, such as the porosity, Gurley number, and tortuosity, are strongly related to ionic conductivity, the unique pore structure of the 3DOM PI separator can provide higher ionic conductivity than the surfactant-coated PP separator.

The thickness of the electrolyte between the anode and cathode is an important parameter that has a significant effect on the internal resistance of cells. To evaluate the electrolytes properly, the conductance of the real electrolytes used in cells should be taken into account. Figure 3–3 (b) shows the Arrhenius plots of the conductance of the electrolytes. The conductance of pristine IG electrolyte, PP–IG composite electrolyte with 25 mm thickness, and 3DOM–IG composite electrolyte with 28 mm thickness were 47.8, 51.0, and 124.5 mS, respectively. The PP–IG composite electrolyte had a higher mechanical strength, but its conductance was lower than that of the pristine IG electrolyte. On the other hand, the 3DOM PI–IG composite electrolyte exhibited both high mechanical strength and conductance compared with other electrolytes. In practical, it can be said that the composite electrolyte between 3DOM-PI and GI is the most promising electrolyte membrane.

3.3.3. Li deposition/dissolution tests

The Li deposition/dissolution performances were evaluated by using Li/Li symmetric cells with three types of electrolytes at various current densities (0.1–1.0 mA cm^{-2}). The area capacity of deposition/dissolution was 0.5 mAh cm^{-2}. Figs 3–4 (a–c) show the voltage profiles during the Li deposition/dissolution at various current densities. The cell employing the pristine IG electrolyte exhibited a rapid decrease in polarization

at 0.5 mA cm^{-2} owing to an internal short circuit. The cells employing the PP–IG and 3DOM PI–IG composite electrolytes did not show the internal short circuit up to 0.3 and 0.7 mA cm^{-2}, respectively. The higher conductance of the 3DOM PI–IG composite electrolyte contributed to Li deposition/dissolution at higher current density. The internal short circuit depends on the thickness of the electrolyte part. The higher current density for the pristine IG electrolyte than that for the PP-IG composite electrolyte was understood by the difference in thickness.

The Li deposition/dissolution cycle performance was investigated at a current density of 0.25 mA cm^{-2} and a deposition/dissolution area capacity of 0.25 mAh cm^{-2}. Figures 3–5 (a–c) show the voltage profiles of the cells employing three types of electrolytes during the Li deposition/dissolution cycle performance tests. The cell employing the pristine IG electrolyte exhibited polarization of 60–70 mV and rapidly decreased at the 10th cycle owing to an internal short circuit. The cell employing the PP–IG and 3DOM PI–IG composite electrolytes exhibited polarization of 100–150 and 50–60 mV, respectively. These results suggest that the introduction of the separator as a framework increases the mechanical strength of the self-standing membrane and suppresses a penetration of Li metal. In addition, the higher conductance of the 3DOM PI–IG composite electrolyte provided a lower polarization, suggesting that the uniform pore structure of the 3DOM PI separator contributed to a more stable Li deposition/dissolution behavior.

The impedance of the cells was measured to investigate the stability of the interface between Li metal and electrolyte/separator. Figures 3–6 (a–c) show the Cole–Cole plots of the Li/Li symmetric cells employing three types of electrolytes at the 1st, 10th, and 50th cycles. The lowest interfacial resistance at the 1st cycle among the prepared

electrolytes was observed when using the pristine IG electrolyte. Probably, a flexibility of pristine IG electrolyte contributes to the formation of good interface between Li metal and electrolyte. The small interface resistance after the 10th cycle may be due to micro short circuit behavior. The cell employing the PP–IG composite electrolyte exhibited unstable interfacial resistance in each cycle, indicating that the interface between Li metal and this electrolyte was not stable. This is related to the unstable Li deposition/dissolution behavior of the cell with PP–IG composite electrolyte. On the other hand, the cell employing the 3DOM PI–IG composite electrolyte exhibited stable interfacial resistance in all cycles, contributing to a stable Li deposition/dissolution behavior.

The deposited Li metal morphology was observed with SEM. The Li/Li symmetric cells were disassembled after the Li deposition/dissolution test, and then the Li metal surface was observed. Figures 3–7 (a–c) show the SEM images of deposited Li in the cell with three types of electrolytes after the 1st cycle. The cells employing the pristine IG electrolyte provided nonuniform Li deposition. This morphology may contribute to a micro short circuit. The cell employing the PP–IG composite electrolyte provided a nonuniform Li deposition owing to the unstable interfacial formation as discussed above. The cells employing the 3DOM PI–IG composite electrolyte provided a uniform Li deposition owing to its unique uniform pore structure, which contributes to the stable interfacial formation and Li deposition/dissolution behavior.

3.3.4. Charge–discharge tests

Charge–discharge tests were performed using the full cells employing the NCM523 cathode and three types of electrolytes. Figures 3–8 (a–c) show the charge–discharge curves of the NCM523/Li full cells at 0.1C (0.2 mA cm^{-2}). The prepared

electrolytes, pristine IG electrolyte, PP–IG composite electrolyte, and 3DOM PI–IG composite electrolyte, exhibited discharge capacities of 80, 105, and 172 mAh g^{-1}, respectively, at the 1st cycle. The low discharge capacities of the full cells employing the pristine IG electrolyte and PP–IG composite electrolyte are due to higher polarization caused by higher internal resistance. In addition, the full cell employing the pristine IG electrolyte was not able to be charged to cut-off voltage. The charging voltage was limited to approximately 3.8 V, which was due to a micro short circuit. On the other hand, the full cell employing 3DOM PI–IG composite electrolyte exhibited an excellent capacity corresponding to the theoretical value of NCM 523 and stable charge–discharge curves.

Figure 3–9 (a) shows the discharge capacity and Fig. 3–9 (b) shows the coulombic efficiency of the charge–discharge tests using the NCM523/Li full cells. The discharge capacity of the full cells employing the pristine IG electrolyte and PP–IG composite electrolyte gradually decreased, while the cells employing the 3DOM–IG composite electrolyte exhibited higher and more stable discharge capacity. The average coulombic efficiencies of the full cells employing the pristine IG electrolyte, PP–IG composite electrolyte, and 3DOM PI–IG composite electrolyte from the 2nd to 20th cycles were 29.18, 95.63, and 99.97 %, respectively. The extremely low coulombic efficiency of full cells with the pristine IG electrolyte was due to a micro short circuit. The low coulombic efficiency of the full cells employing the PP–IG composite electrolyte suggested more active undesirable reactions, mainly electrolyte decomposition. Nonuniform Li deposition promotes a breaking down solid electrolyte interphase (SEI) layer which can produce a fresh Li metal surface. This contributes to further reactions with electrolytes, leading to a more unstable interface between the Li metal and separator/electrolyte. On the other hand, the full cells employing 3DOM PI–IG composite

electrolyte exhibited higher and more stable coulombic efficiency owing to more uniform Li deposition. The unique and uniform pore structure of the 3DOM PI separator provides a more uniform Li^+ ion flux and current distribution, which contributes to the more uniform Li deposition. The reactivity of the 3DOM PI separator with IG electrolytes is lower than that of the 3DOM PI separator with ILEs, owing to the lower fluidity of gel electrolytes. The 3DOM PI–IG composite electrolyte is the best electrolyte for Li metal anode.

3.4. Conclusion

The surfactant-coated PP and 3DOM PI separators were introduced as a framework for the pristine IG electrolyte. The separator improved the mechanical strength of the IG electrolyte membrane, so that the self-standing membranes were successfully prepared. The improvement of the mechanical strength suppressed an internal short circuit owing to the nonuniform Li deposition/dissolution behavior. In particular, the 3DOM PI–IG composite electrolyte membrane exhibited highly stable Li deposition/dissolution behavior. The NCM523/Li full cell composed with the 3DOM PI–IG composite electrolyte exhibited higher coulombic efficiency and cycle performance. The high porosity and uniform porous structure of the 3DOM PI separator provided higher conductance of the electrolyte layer, leading to more uniform Li deposition/dissolution behavior owing to more uniform interface formation between Li metal and electrolyte. The composite of the 3DOM PI separator and IG electrolyte was useful to improve the trade-off relationship between ionic conductivity and mechanical strength of the IG self-standing membrane.

Table 1. Physical properties of the surfactant-coated PP and the 3DOM PI separator.

	Tickness [μm]	Pore size [nm]	Porosity [%]	Gurley number [s cm^{-3}]
3DOM PI	**28**	**300 (75)**	**75**	**160**
Surfactant-coated PP	**25**	**43**	**41**	**620**

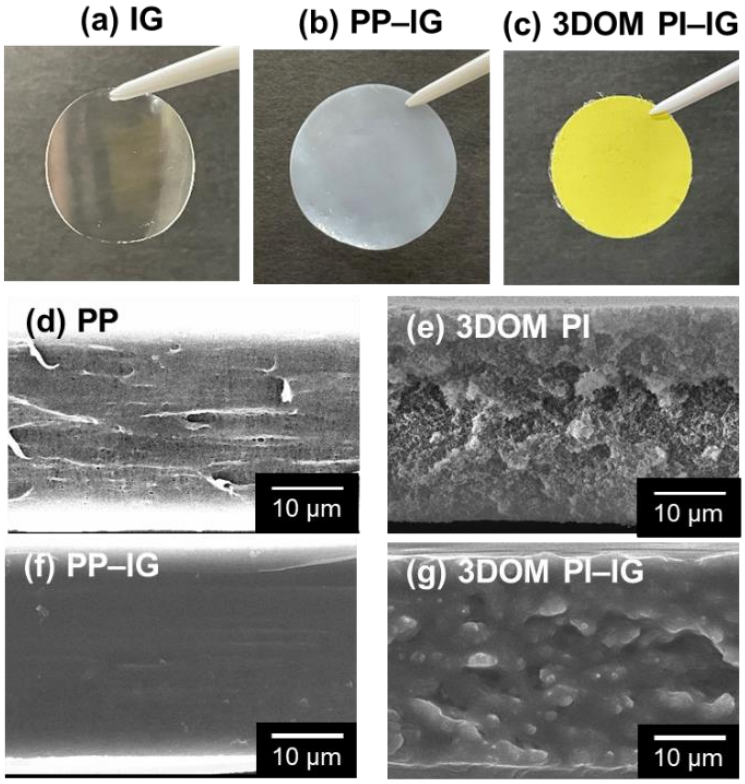

Figure 3–1. Photograph of prepared electrolytes: (a) pristine IG electrolyte, (b) PP–IG composite electrolyte, and (c) 3DOM PI–IG composite electrolyte. Cross-section SEM images of (d) surfactant-coated PP separator, (e) 3DOM PI separator, (f) PP–IG composite electrolyte, and (g) 3DOM PI–IG composite electrolyte.

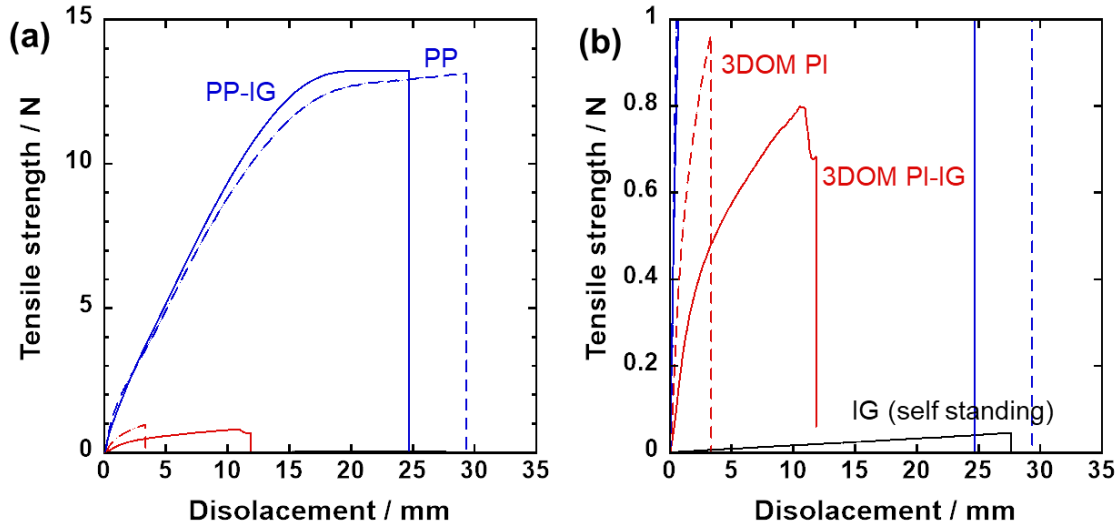

Figure 3–2. Stress-strain curves of (a) PP–IG electrolyte and (b) pristine IG electrolyte and 3DOM PI–IG electrolyte.

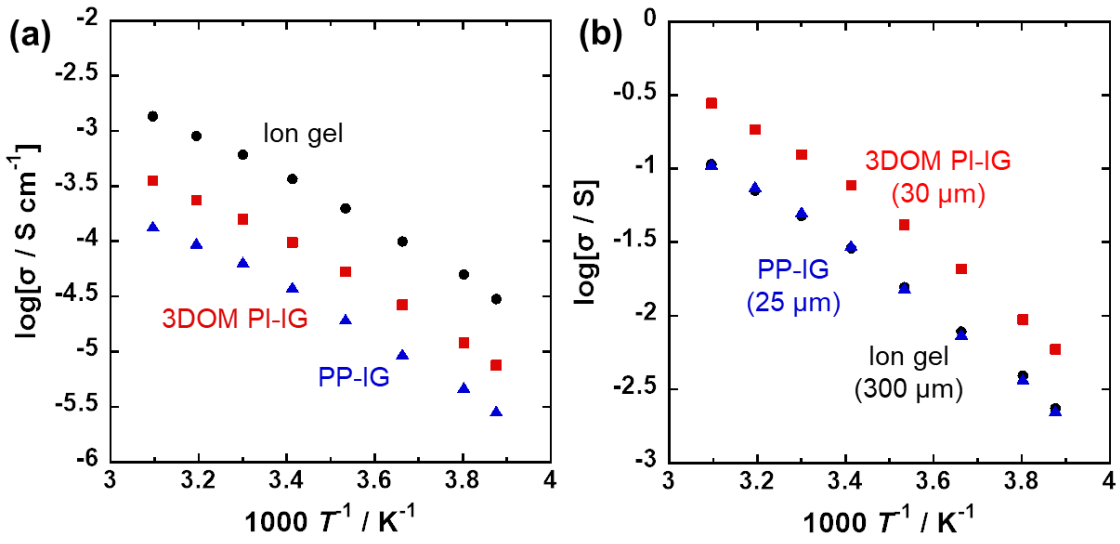

Figure 3–3. Arrhenius plots of (a) ionic conductivities and (b) conductance of three types of electrolytes: pristine IG electrolyte, PP–IG electrolyte, and 3DOM PI–IG electrolyte.

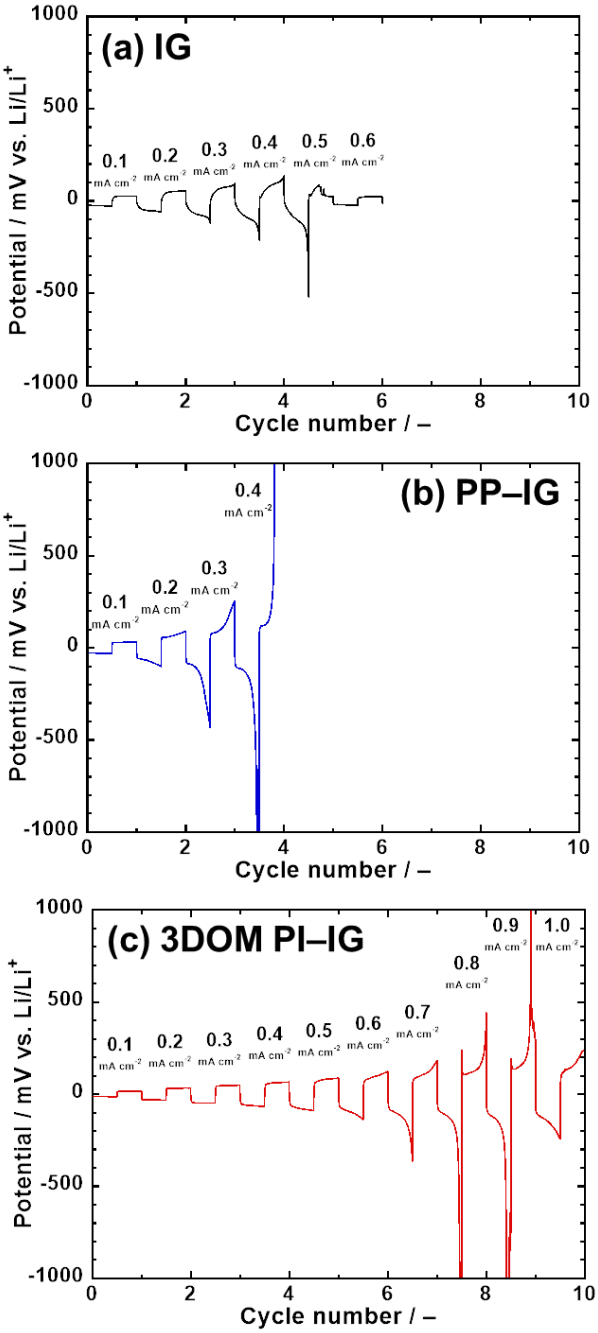

Figure 3–4. Voltage profiles of Li deposition/dissolution test using Li/Li symmetric cells at various current densities employing (a) pristine IG electrolyte, (b) PP–IG composite electrolyte, and (c) 3DOM PI–IG composite electrolyte.

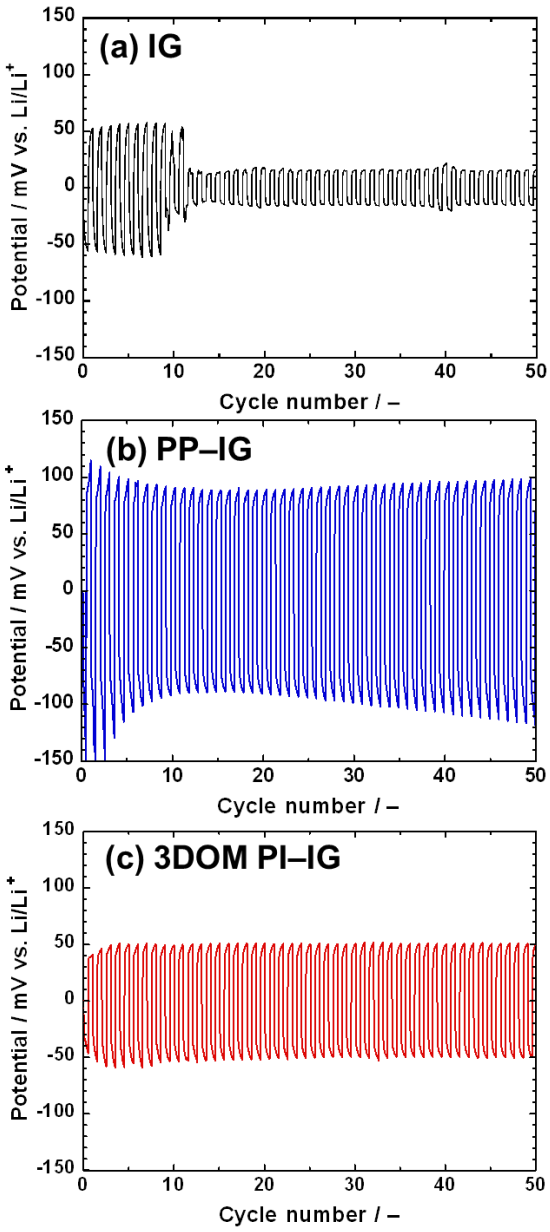

Figure 3–5. Voltage profiles of Li deposition/dissolution test using the Li/Li symmetric cells employing (a) pristine IG electrolyte, (b) PP–IG composite electrolyte, and (c) 3DOM PI–IG composite electrolyte.

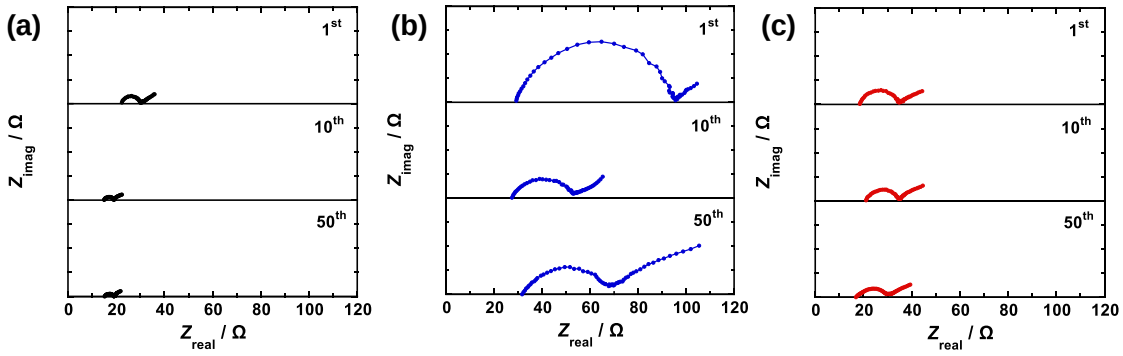

Figure 3–6. Cole–Cole plots during Li deposition/dissolution cycles using the Li/Li symmetric cells employing (a) pristine IG electrolyte, (b) PP–IG composite electrolyte, and (c) 3DOM PI–IG composite electrolyte.

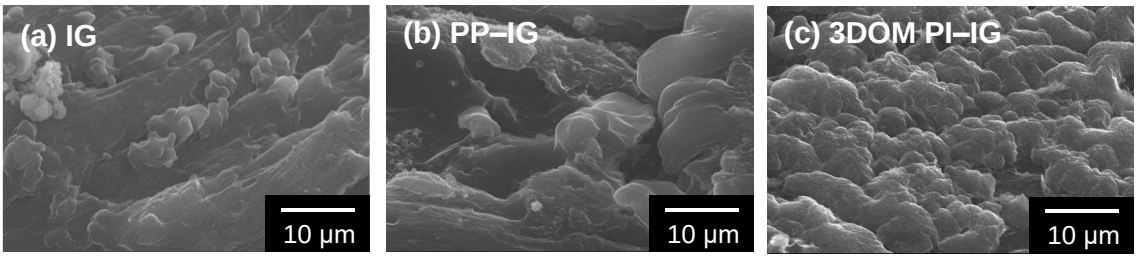

Figure 3–7. SEM images of the surface of deposited Li in the Li/Li symmetric cells employing (a) pristine IG electrolyte, (b) PP–IG composite electrolyte, and (c) 3DOM PI–IG composite electrolyte.

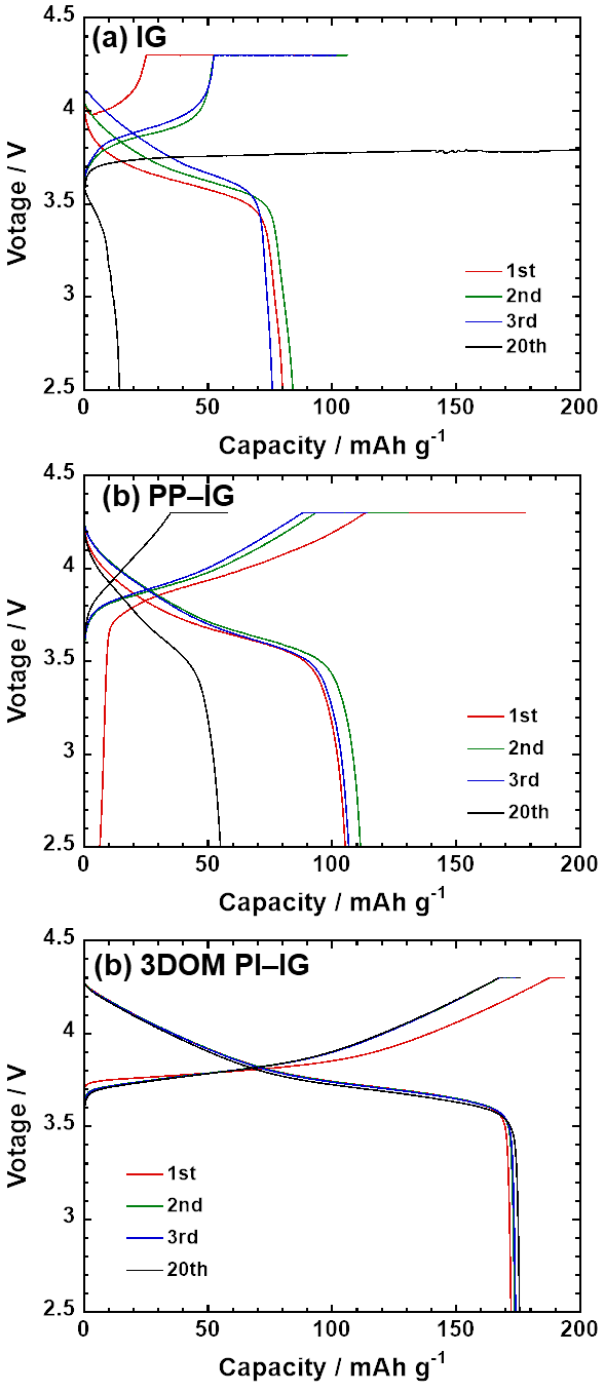

Figure 3–8. Charge–discharge curves of the NCM523/Li full cells employing (a) pristine IG electrolyte, (b) PP–IG composite electrolyte, and (c) 3DOM PI–IG composite electrolyte.

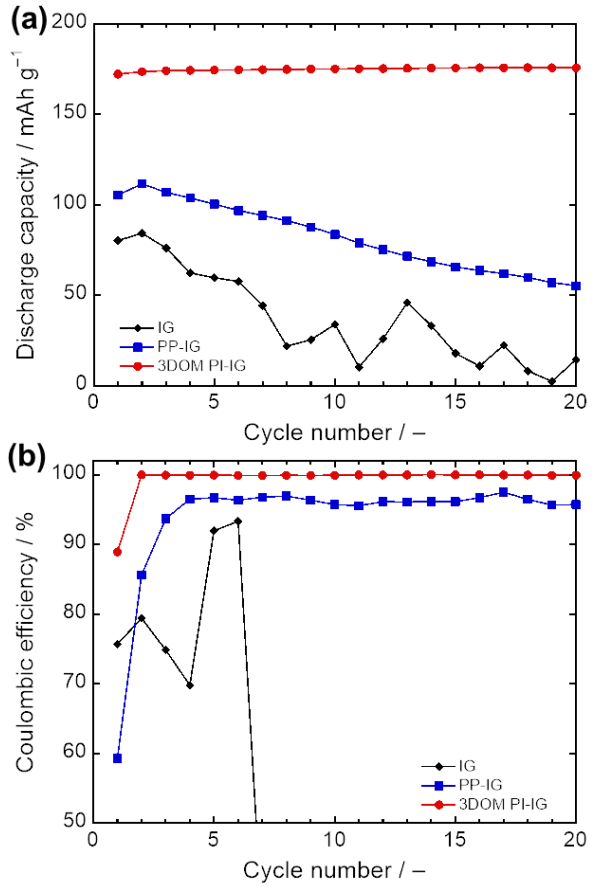

Figure 3–9. (a) Discharge capacity and (b) Coulombic efficiency of the NCM523/Li full cells.

3.5. References

1. J. M. Tarascon, and M. Armand, Nature, 414, 359 (2001)
2. W. Xu, J. L. Wang, F. Ding, X. L. Chen, E. Nasybutin, Y. H. Zhang, and J. G. Zhang, Energy Environ. Sci., 7, 513 (2014)
3. D. C. Lin, Y. Y. Liu, and Y. Cui, Nat. Nanotechnol., 12, 194 (2017)
4. M. Ue, and K. Uosaki, Curr. Opin. Electrochem., 17, 106 (2019)
5. D. P. Lu, Y. Y. Shao, T. Lozano, W. D. Bennett, G. L. Graff, B. Polzin, J. G. Zhang, M. H. Engelhard, N. T. Saenz, W. A. Henderson, P. Bhattacharya, J. Liu, and J. Xiao, Adv. Energy Mater., 5, 1400993 (2015)
6. J. Liu, Z. N. Bao, Y. Cui, E. J. Dufek, J. B. Goodenough, P. Khalifah, Q. Y. Li, B. Y. Liaw, P. Liu, A. Manthiram, Y. S. Meng, V. R. Subramanian, M. F. Toney, V. V. Viswanathan, M. S. Whittingham, J. Xiao, W. Xu, J. H. Yang, X. Q. Yang, and J. G. Zhang, Nat. Energy, 4, 180 (2019)
7. K. Xu, Chem. Rev., 104, 4303 (2004)
8. A. J. Nagajothi, R. Kannan, and S. Rajashabala, Polym. Bull., 74, 4887 (2017)
9. D. Ding, Y. Maeyoshi, M. Kubota, J. Wakasugi, K. Kanamura, and H. Abe, J. Power Sources, 506 (2021)
10. K. Elamin, M. Shojaatalhosseini, O. Danyliv, A. Martinelli, and J. Swenson, Electrochimica Acta, 299, 979 (2019)
11. X. Y. Shi, Q. W. Sun, B. Boateng, Y. H. Niu, Y. D. Han, W. Q. Lv, and W. D. He, J. Power Sources, 414, 225 (2019)
12. S. Kuwabata, and M. Tomiyori, J. Electrochem. Soc., 149, A988 (2002)
13. A. Hosseinioun, P. Nuernberg, M. Schoenhoff, D. Diddens, and E. Paillard, RSC Advances, 9, 27574 (2019)

14. Q. Yang, N. P. Deng, J. Y. Chen, B. W. Cheng, and W. M. Kang, Chem. Eng. J., 413, 127427 (2021)

15. A. Lewandowski, and A. Świderska-Mocek, J. Power Sources, 194, 601 (2009)

16. M. Watanabe, M. L. Thomas, S. Zhang, K. Ueno, T. Yasuda, and K. Dokko, Chem Rev, 117, 7190 (2017)

17. H. Matsumoto, H. Sakaebe, K. Tatsumi, M. Kikuta, E. Ishiko, and M. Kono, J. Power Sources, 160, 1308 (2006)

18. G. B. Appetecchi, M. Montanino, M. Carewska, M. Moreno, F. Alessandrini, and S. Passerini, Electrochimica Acta, 56, 1300 (2011)

19. M. Eftekharnia, M. Hasanpoor, M. Forsyth, R. Kerr, and P. C. Howlett, ACS Appl. Energy Mater., 2, 6655 (2019)

20. T. Evans, J. H. Lee, V. Bhat, and S. H. Lee, J. Power Sources, 292, 1 (2015)

21. H. Yoon, P. C. Howlett, A. S. Best, M. Forsyth, and D. R. MacFarlane, J. Electrochem. Soc., 160, A1629 (2013)

22. R. Furuya, T. Hara, T. Fukunaga, K. Kawakami, N. Serizawa, and Y. Katayama, J. Electrochem. Soc., 168, 100516 (2021)

23. M. Watanabe, S. Yamada, K. Sanui, and N. Ogata, Journal of the Chemical Society-Chemical Communications, 929 (1993)

24. M. Freemantle, Chem. Eng. News, 82, 26 (2004)

25. X. W. Li, Y. W. Zheng, and C. Y. Li, Energy Storage Materials, 29, 273 (2020)

26. K. Hashimoto, R. Tatara, K. Ueno, K. Dokko, and M. Watanabe, J. Electrochem. Soc., 168 (2021)

27. J. Jang, J. Oh, H. Jeong, W. Kang, and C. Jo, Materials, 13, 4625 (2020)

28. Y. Shimizu, and K. Kanamura, J. Electrochem. Soc., 166, A754 (2019)

29. Y. Shimizu, and K. Kanamura, Chem. Lett., 48, 429 (2019)

30. R. Miyagawa, J. Takeyoshi, K. Kanamura, S. Taminato, D. Mori, and N. Imanishi, Electrochemistry, 90, 107005 (2022)

31. J. Takeyoshi, N. Kobori, and K. Kanamura, Electrochemistry, 88, 540 (2020)

32. Y. Shimbori, K. Nishikawa, K. Kajihara, and K. Kanamura, Electrochemistry, 91, 127003 (2023)

33. P. G. Bruce, and C. A. Vincent, J. Electroanal. Chem. Interfacial Electrochem., 225, 1 (1987)

34. J. Evans, C. A. Vincent, and P. G. Bruce, Polymer, 28, 2324 (1987)

35. P. G. Bruce, Solid State Ionics, 28-30, 918 (1988)

36. V. Mauro, A. D'Aprano, F. Croce, and M. Salomon, J. Power Sources, 141, 167 (2005)

37. H. Vogel, Phys. Z., 22, 645 (1921)

38. G. Tammann, and W. Hesse, Z. Anorg. Allg. Chem., 156, 245 (1926)

39. G. S. Fulcher, J. Am. Ceram. Soc., 8, 339 (1925)

40. C. A. Angell, The Journal of Physical Chemistry, 68, 1917 (1964)

41. A. Noda, K. Hayamizu, and M. Watanabe, J. Phys. Chem. B, 105, 4603 (2001)

42. W. Xu, E. I. Cooper, and C. A. Angell, J. Phys. Chem. B, 107, 6170 (2003)

Chapter 4: Effect of Polybenzimidazole Addition to Three-Dimensionally Ordered Macroporous Polyimide Separators on Mechanical Properties and Electrochemical Performances

4.1. Introduction

Li-ion batteries exhibit the highest energy density among rechargeable batteries in practical applications. Recently, next-generation batteries employing active materials with higher capacities have attracted attention. In particular, Li metal is the ultimate anode material owing to the highest theoretical capacity density of 3861 mAh g^{-1}, which is 10 times larger than that of a graphite anode (372 mAh g^{-1}). [1] Furthermore, the Li-metal anode can provide a larger operation voltage of the cell owing to the lowest redox potential (–3.04 V vs. SHE) of Li metal. Therefore, Li-metal batteries employing Li-metal anodes have been widely studied. [2–4] However, Li metal undergoes nonuniform deposition promoting a low coulombic efficiency and an internal short circuit resulting in a lower battery safety.

Various approaches have been investigated to solve these problems. The Li deposition morphology and the solid electrolyte interphase (SEI) layers were investigated most intensively. [5–8] These studies reveal that a more stable and uniform SEI layer provides a higher coulombic efficiency owing to the suppression of electrolyte decomposition and the prevention of a large distribution of electrode reactions. Several studies have prepared more uniform and stable SEI layers by changing the type of electrolyte and using additives. [9–15] In addition, the morphology of the deposited Li metal

significantly affects the stabilization of the SEI layer. Owing to volume and morphology changes, SEI layers with low mechanical strength are physically damaged during the Li deposition/dissolution process. Large granular deposited Li prevents side reactions with electrolytes and damage to the SEI layer owing to volume changes. [16,17] Another approach, such as the influence of external pressure on the cells, stabilizes the Li-metal anode. [18–20] The application of external pressure to the cells resulted in the formation of dense Li-metal deposits and improved cycle performances.

By contrast, we focused on the Li^+ ion flux in the separators to reduce reaction distribution in the electrodes. The separator contacts the Li-metal anode, strongly affecting Li deposition/dissolution behavior. [21,22] The uniform deposition of Li metal was observed when the Li^+ ion flux in the separator was uniform. However, conventional polyolefin separators have a nonuniform pore structure and they promote nonuniform reaction distribution in the electrode. To solve this problem, we have developed an ultrafine porous polyimide membrane with an inverse opal structure. [23–26] This membrane has been used as a three-dimensionally ordered microporous polyimide (3DOM PI) separator, which has been applied to the Li-metal anode to improve cycle performance. [27–32] The 3DOM PI separator provides better Li deposition/dissolution cycle performance owing to its unique and uniform pore structure. However, the mechanical strength of the 3DOM PI separator is still low, and this results in a compression of pores in the separator when external pressure is applied to cells.

In this study, we added polybenzimidazole (PBI) to increase the mechanical strength of the 3DOM PI separator. PBI is an engineering plastic, similar to PI, and has higher mechanical strength and thermal stability than PI. In the previous report, smaller pores in the 300–800 nm range have exhibited better Li deposition/dissolution and

charge–discharge performances. [29] In this study, pore sizes of 300 and 100 nm were prepared to make clear more detailed effects of pore size on the Li deposition/dissolution process. The physical properties of the four separators were investigated in terms of their tensile strength, thermal stability, and gas permeability. Subsequently, Li deposition/dissolution cycle tests were conducted to investigate the cycling performance of the Li-metal anodes. Finally, the charge–discharge cycle tests were performed using cells with a $LiNi_{0.5}Co_{0.2}Mn_{0.3}O_2$ (NCM523) cathode and a Li-metal anode. The effect of the addition of PBI and pore size was investigated by using a highly concentrated electrolyte. This electrolyte has provided a better cycling performance.[31]

4.2. Experimental

4.2.1. Preparation procedure of 3DOM PI and PI+PBI separators

The 3DOM PI and PI+PBI separators were prepared using a colloidal crystalline template method with mono-disperse silica particles. Figures 4–1 (a) and (b) show the structural formula of PI and PBI. Polyamic acid (JVI-2002, JFE Chemical Corp.) was used as the precursor for the PI. PBI was purchased from SATO LIGHT INDUSTRIAL Co., Ltd.. Mono-disperse silica spherical particles (Seahostar® KE-P, Nippon Shokubai Co., Ltd.) were used as template particles. The 3DOM PI separators contained 0 wt% PBI, and the 3DOM PI+PBI separators contained 10 wt% PBI. These materials were dispersed in *N*,*N*-dimethylacetamide (Wako Special Grade; Fujifilm Wako Pure Panaca Co., Ltd.) to prepare a slurry. The slurry was coated on PET films (PANA-PEEL®NP-75-A, Panac Co., Ltd.) and dried to remove the solvent. The precursor sheet was imidized by heating at 320 °C for 2 h. The remaining silica particles in the sheet were removed using a 10 wt% aqueous hydrofluoric acid solution. The resulting 3DOM PI and 3DOM PI+PBI

separator were dried under vacuum at 120 °C for 48 h.

4.2.2. Preparation procedure of the electrolyte

$[LiFSI]_1[EC]_2$ was prepared from Li bis(fluorosulfonyl)imide (LiFSI, KISHIDA CHEMICAL CO., Ltd.) and ethylene carbonate (EC, KISHIDA CHEMICAL CO., Ltd.). LiFSI and EC were mixed in a molar ratio of 1:2. The water contents of the prepared electrolytes were analyzed using the Karl Fischer titration method (Kyoto Electronic Manufacturing Co., Ltd., MKC-710). The water content was < 50 ppm.

4.2.3. Characterization of the separators and Li-metal anode

The morphologies of the separators and Li metal were observed using scanning electron microscopy (SEM) (JSM-6490A, JEOL Ltd.). The thermal stability of the separators was measured by thermogravimetric analysis (TGA) (DTG-60H, SHIMADZU Corp.) in air up to 600 °C with a heating rate of 5 °C/min. The mechanical strength and gas permeability of the separators were measured by using a tensile tester (Autograph AGS-X, SHIMADZU Corp) and a Gurley permeabilities tester (No. 158 GURLEY TYPE DENSOMETER, TOYOSEIKI Co., Ltd.), respectively.

4.2.4. Transference number measurement

The cationic transference numbers t_+ of the electrolyte in the separators were calculated using a frequency response analyzer built-in potentiostat/galvanostat (VMP-300, BioLogic Science Instruments) and the following Equation (1),

$$t_+ = i_s(\Delta V - i_0 R_0) / i_0(\Delta V - i_s R_s) \quad (1)$$

where ΔV is the applied voltage, i is the current, and R is the sum of the charge transfer

resistance and passivation film resistance. Subscripts 0 and s indicate the initial and steady-state values, respectively. [33-36] The ΔV was set at 5 mV. The impedance measurement was performed using alternating current (AC) voltage with ±5 mV amplitude in the frequency ranges of 1 MHz to 50 mHz.

4.2.5. Ionic conductivity measurement

The ionic conductivities of the electrolytes in the separators were measured using the 2032-type coin cells with Au electrodes and a frequency response analyzer built-in potentiostat/galvanostat (VMP-300). Electrochemical impedance spectroscopy (EIS) was performed using AC voltage with ±5 mV amplitude in the frequency ranges of 100 kHz to 100 mHz. The ionic conductivity, σ (S cm^{-1}), was determined using Equation (2) as follows:

$$\sigma = d/(R_b S), \quad (2)$$

where d denotes the separator thickness (cm), R_b is the bulk resistance (Ω) measured by EIS, and S is the electrode area (cm^2). The measurements were performed in the temperature range of 20–60 °C to obtain Arrhenius plots of the ionic conductivity.

4.2.6. Li deposition/dissolution test of Li/Li symmetric cells

The Li/Li symmetric cells were constructed in a glovebox filled with Ar gas using Li foil on the Cu current collector (100 μm Li/10 μm Cu, Honjo Metal Co., Ltd.), $[LiFSI]_1[EC]_2$ electrolyte, and 3DOM PI or PI+PBI separator with pouch cells.

Li deposition/dissolution tests were performed using Li/Li symmetric cells at a current density of 10 mA cm^{-2} for 30 min at 30 °C using charge–discharge test equipment (TOSCAT-3100, TOYO SYSTEM Co., Ltd.). This current density was employed. The

higher current density generally provides a more uniform Li deposition/dissolution behavior and better cycle performance. The cell impedances for Li/Li symmetric cells were measured using a frequency response analyzer built-in potentiostat/galvanostat (VMP-300) with AC voltage with ±5 mV amplitude in the frequency ranges of 1 MHz to 50 mHz.

4.2.7. Charge–discharge test of full cells

$LiNi_{0.5}Mn_{0.2}Co_{0.3}O_2$ (NCM523)/Li full cells were constructed in a glovebox filled with Ar gas. NCM523 electrode sheet (bcaf-ncm523ss, MTI Corp.) with 2 mAh cm^{-2} was used as the cathode. Li foil on the Cu current collector (20 μm Li/10 μm Cu, Honjo Metal Co., Ltd.) was used as the anode. $[LiFSI]_1[EC]_2$ was used as an electrolyte. 3DOM PI or PI+PBI separator was used in the pouch cell with NCM523 and Li.

The charge–discharge test of NCM523/Li full cells was performed in the voltage range of 2.5–4.3 V with constant current-constant voltage mode for charging and constant current mode for discharging at 30 °C using charge–discharge test equipment (TOSCAT-3100, TOYO SYSTEM Co., Ltd.). The test was performed at 0.1 C rate for the initial three cycles and then at 0.2 C rate after the 4th cycle. The rest for the 48 hours was included after the 70th cycle in this cycle test.

4.3. Results and discussion

4.3.1. Properties of separators

Figures 4–2 (a–d) show the SEM images of the surface morphology of the separators. All the separators had uniform pore structures and controlled pore sizes of approximately 300 or 100 nm, depending on the template particle size from SEM images.

Figs. 4–2 (e–h) show SEM images of the cross sections of the separators. Highly uniform and a controlled pore size was confirmed. Porosities of 3DOM PI (300 nm), PI (100 nm), PI+PBI (300 nm), and PI+PBI (100 nm) were 77.9%, 76.2%, 74.2%, and 74.0%, respectively, as listed in Table 1. The 3DOM PI separators exhibit higher porosities than a theoretical value of hexagonal closed-packed structures (74.0 %) owing to a volume shrinkage of PI during the preparation process. This volume change was suppressed by the addition of PBI, leading to the theoretical value of porosity. Gurley numbers of 3DOM PI (300 nm), PI (100 nm), PI+PBI (300 nm), and PI+PBI (100 nm) were 45.8, 138.8, 88.0, and 166.5 s 100 cm^{-3}, respectively, as listed in Table 1. Gas permeability was higher for the 3DOM PI separators than for the 3DOM PI+PBI ones, and for the 3DOM separators with 300 nm pores than for those with 100 nm pores. The Gurley numbers depended on the size of the connecting pores, suggesting that the suppression of shrinkage during the separator preparation process by the addition of PBI resulted in a smaller connecting pore size.

TGA was performed to investigate the effect of the addition of PBI on the thermal stability of the 3DOM separators, as shown in Fig. 4–3. The weights of 3DOM PI (300 nm), PI (100 nm), PI+PBI (300 nm), and PI+PBI (100 nm) notably decreased at 470, 420, 500, and 490 °C, respectively, because of the combustion of PI. The residual weight at 600 °C was approximately 10 wt% for the 3DOM PI+PBI separator and was attributed to PBI. These results suggest that the addition of PBI improved the thermal stability of the 3DOM separator. Furthermore, the weight loss of the 3DOM PI separator from room temperature may be due to the desorption of absorbed water and DMAc, indicating that the 3DOM PI separator must be sufficiently dried before use.

The effect of pore size and the addition of PBI on the tensile strength of the

separators were investigated, as shown in Fig. 4–4. The tensile strengths of 3DOM PI (300 nm), PI (100 nm), PI+PBI (300 nm), and PI+PBI (100 nm) were 9.1, 8.0, 20.6, and 15.3 MPa, respectively. The displacements were 4.3, 3.3, 6.4, and 5.1 mm, respectively. The 3DOM PI+PBI separators exhibited higher tensile strengths and larger displacements than the 3DOM PI separators. The 3DOM separators with 300 nm pores exhibited higher tensile strength and larger displacement than those with 100 nm pores owing to the larger average thickness of the 3DOM framework.

Figure 4–5 shows the Arrhenius plots of ionic conductivity of the separators with $[LiFSI]_1[EC]_2$, evaluated using EIS measurement at various temperatures. Ionic conductivities at 30 °C of highly concentrated electrolyte without separators, with 3DOM PI (300 nm), 3DOM PI (100 nm), 3DOM PI+PBI (300 nm), and 3DOM PI+PBI (100 nm), were 1.59, 0.80, 0.54, 0.45, and 0.39 mS cm^{-1}, respectively. Ionic conductivities were higher for the 3DOM separators with 300 nm pores than for those with 100 nm pores, and for the 3DOM PI separators than for the 3DOM PI+PBI separators. These results are consistent with the notion that the Gurley number is strongly related to ionic conductivity.[22,37] The activation energies of highly concentrated electrolyte without separators, with 3DOM PI (300 nm), 3DOM PI (100 nm), 3DOM PI+PBI (300 nm), and 3DOM PI+PBI (100 nm), were 29.7, 21.8, 17.2, 16.4, and 15.9 kJ mol^{-1}, respectively. The different activation energies suggest different ion conduction mechanisms. The Li^+ transference numbers of those separators were 0.57, 0.60, 0.62, 0.77, and 0.78, respectively, as listed in Table 1, and increased with decreasing activation energy. This also suggests that the interaction between the highly concentrated electrolyte and 3DOM separators influences the ion conduction mechanisms. However, a previous study for a conventional electrolyte (1M $LiPF_6$/EC) without separators and with 3DOM PI separators reported the same slope

of the Arrhenius plots. [29] From these results, it is confirmed that the interaction between the electrolyte and the 3DOM PI separator is greatly affected by the types of electrolytes. PI may interact with Li^+ ions, which affect the formation of contact ion pair (CIP) and aggregate (AGG), Li^+ transference numbers, and ion conductive mechanisms of the highly concentrated electrolyte in the separators. The addition of PBI may influence the interaction between Li^+ ions and the polymer matrix, resulting in ion conduction mechanisms.

4.3.2. Li deposition/dissolution performance

Figures 4–6 (a–d) show the voltage profiles of Li/Li symmetric cells during the Li deposition/dissolution cycles. The capacity for the Li deposition/dissolution cycle was 5 mAh cm^{-2} and the current density was 10 mA cm^{-2}. All cells employing the 3DOM separators exhibited stable Li deposition/dissolution behavior over 500 cycles. The 3DOM PI (300 nm) separator provided a polarization of 30 mV for up to 200 cycles and 50 mV after 200 cycles. The 3DOM PI (100 nm) separator provided a polarization of 60–80 mV. The 3DOM PI+PBI (300 nm) and 3DOM PI+PBI (100 nm) separators provided a polarization of 30 and 25 mV, respectively. The 3DOM PI+PBI separators exhibited lower polarization and better polarization stability than the 3DOM PI separators.

Figures 4–7 (a–d) show the Cole–Cole plots of the Li/Li symmetric cells after the 1st, 50th, and 100th cycles. Capacitive semicircles were observed in all the plots. In the 3DOM PI separators, the bulk resistance at the 1st cycle was lower in the separator with 300 nm pores than in the one with 100 nm pores, consistent with their ionic conductivity. In these separators, the bulk resistances at the 50th and 100th cycles were higher than those at the 1st cycle. The 3DOM PI+PBI separators exhibited better bulk and

interfacial resistances stability than the 3DOM PI separators. Furthermore, the bulk resistances almost unchanged up to 100 cycles. The separator with 300 nm pores exhibited slightly higher bulk and interfacial resistances than those with 100 nm pores owing to the effect of the deposited Li surface area.

After 100 cycles of the Li deposition/dissolution test, the cells were disassembled, and the Li metal was observed by SEM. Figures 4–8 (a–d) show the SEM images of the surface of the deposited Li metal. Granular Li particles were observed on the Li surface of all the cells. The 3DOM separators with 300 nm pores provided a slightly larger granular Li than those with 100 nm pores. This suggests that the pore size of the 3DOM separators affects the size of the deposited Li. Furthermore, the 3DOM PI+PBI separators provided a larger granular Li than the 3DOM PI separators.

The addition of PBI to the 3DOM PI separators resulted in lower polarization and bulk resistances in Li dissolution/deposition tests. The increase in the mechanical strength of the separators prevented compression of the pores in the separators by external pressure, leading to a preservation of ionic conduction pathways. This contributed to the improving apparent ionic conductivity of the electrolyte inside the separator and a more uniform reaction distribution. Furthermore, the pore size of separators affects the size of deposited Li.[29] The larger granular Li with smaller surface area enable stable polarization and internal resistance owing to the suppression of side reactions between the deposited Li and the electrolyte.

4.3.3. Charge–discharge performance

Charge–discharge cycle performance tests of NCM523/Li full cells were conducted to investigate the effect of the cathode on the charge–discharge behaviors.

Figures 4–9 (a) and (b) show the charge–discharge curves at the 4th and 100th cycles, respectively, and Figs. 4–10 (a) and (b) show the discharge capacities and coulombic efficiencies of the charge–discharge cycle performance tests. The charge–discharge curves of the cells employing 3DOM PI (300 nm), PI (100 nm), PI+PBI (300 nm), and PI+PBI (100 nm) at the 4th cycle exhibited nearly the same behavior and their discharge capacities were 151.6, 155.2, 152.5, and 155.1 mAh g^{-1}, respectively. Polarization of these cells in the charge–discharge curves at the 100th cycle was larger than those at the 4th cycle. The discharge capacities at the 100th cycle were 106.2, 118.3, 128.9, and 144.7 mAh g^{-1}, respectively. The 3DOM PI+PBI separators exhibited better cycle performance than the 3DOM PI separators. This suggests that the addition of PBI improves the mechanical strength of the separator and suppresses the compression of pores in the separator, providing a more uniform ion flux inside the separator and rection distribution on the electrodes. Furthermore, the 3DOM PI+PBI (100 nm) separator provided the best cycling performance for the full cells. Separators with smaller pore sizes may provide a more uniform reaction distribution. The average coulombic efficiencies of the cells with 3DOM PI (300 nm), PI (100 nm), PI+PBI (300 nm), and PI+PBI (100 nm) between the 4th and 100th cycles were 99.08, 99.25, 99.32, and 99.36%, respectively. The coulombic efficiency was higher in the 3DOM PI+PBI separator than in the 3DOM PI separator, again indicating that more uniform reaction distribution on the electrode and suppressed side reactions with the electrolyte. The discharge capacity degradation started after the rest in the 70th cycle. The capacity degradation after the 70th cycle could be attributed to electrolyte depletion, which was expected from the coulombic efficiency.

4.4. Conclusion

PBI was added to a 3DOM PI separator to increase its mechanical strength. Four types of separators were prepared using two materials, PI and PI+10 wt% PBI, and two types of template particles, 300 and 100 nm, and their physical and electrochemical properties are also investigated. The 3DOM PI separator exhibited a higher porosity and Gurley number, while the 3DOM PI+PBI separator exhibited higher tensile strength and thermal stability. Furthermore, the 3DOM PI+PBI separator showed a more stable Li deposition/dissolution and charge–discharge cycle performance of the full cell than the 3DOM PI separator. An increase in the mechanical strength of the separator prevented the compression of pores in the separator by external pressure, and provided a more uniform reaction distribution in the electrodes. The pore size of the 3DOM PI+PBI separators also affected the size of granular Li. The 3DOM PI+PBI (100 nm) separator provided smaller granular Li but a more uniform electrode reaction distribution, which resulted in better charge–discharge cycle performance of the full cell.

Table 1. Physical and electrochemical properties of separators.

	Thickness / μm	Porosity / %	Gurley number / s 100 cm^{-3}	Li^+ transference number
$[LiFSI]_1[EC]_2$	–	–	–	0.57
3DOM PI (300 nm)	20	77.9	45.8	0.60
3DOM PI (100 nm)	20	76.2	138.8	0.62
3DOM PI+PBI (300 nm)	20	74.2	88.0	0.77
3DOM PI+PBI (100 nm)	20	74.0	166.5	0.78

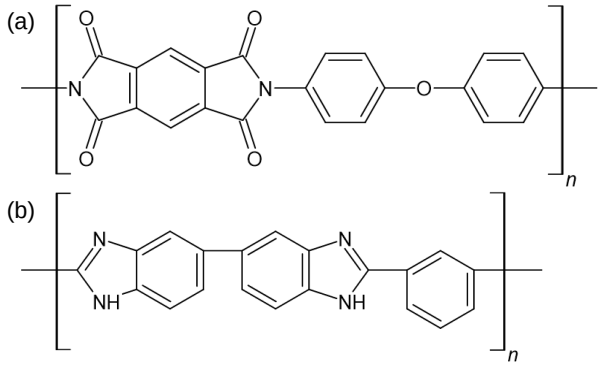

Figure 4–1. Structural formula of (a) PI and (b) PBI.

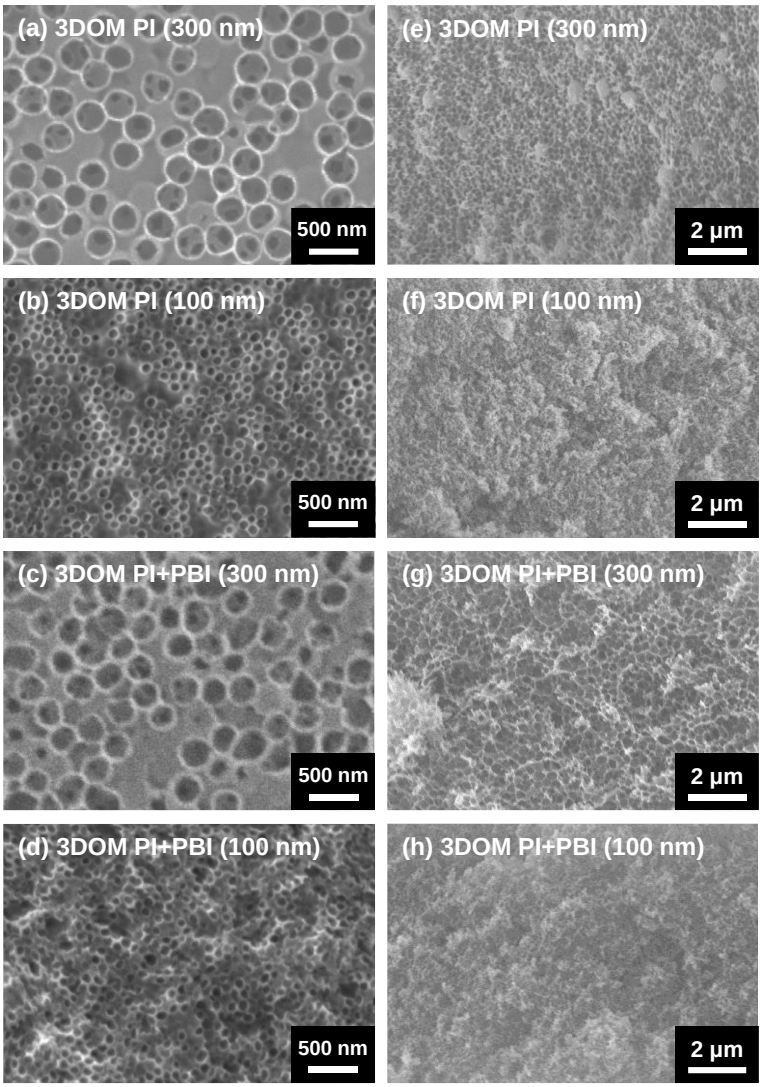

Figure 4–2. SEM images of (a–d) surface and (e–h) cross section of 3DOM PI and 3DOM PI+PBI separators.

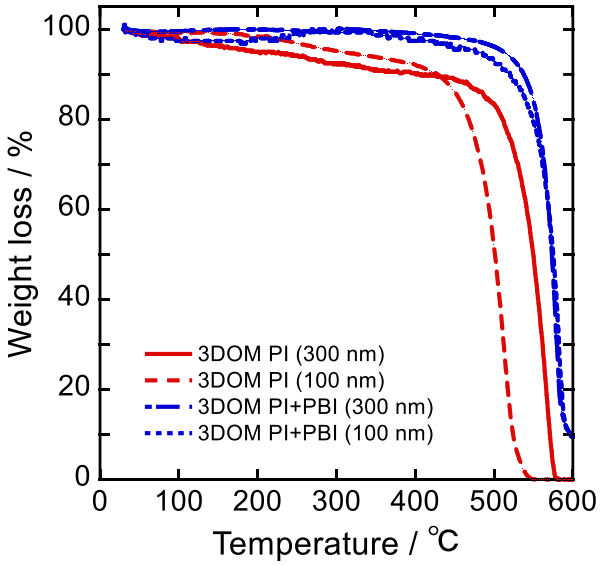

Figure 4–3. TGA curves of 3DOM PI and 3DOM PI+PBI separators.

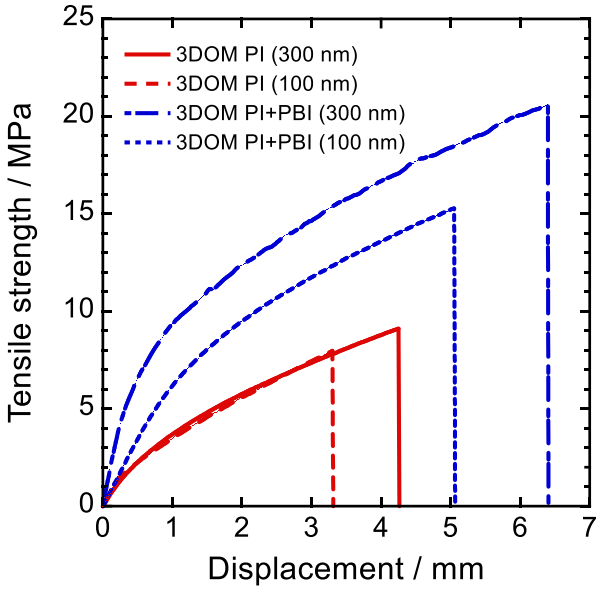

Figure 4–4. Stress–strain curves of 3DOM PI and 3DOM PI+PBI separators.

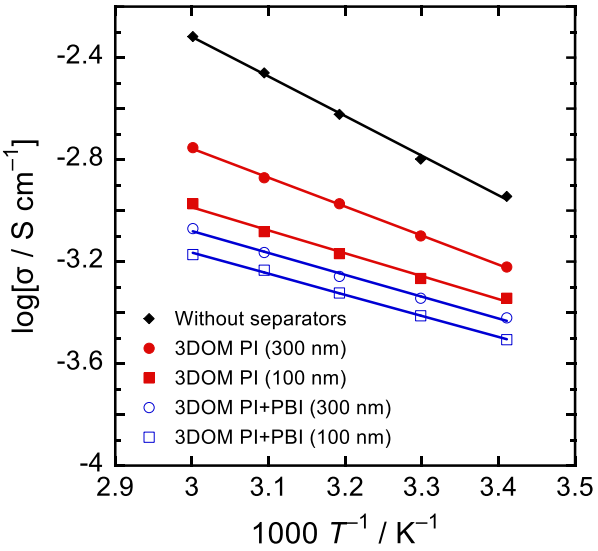

Figure 4–5. Arrhenius plots of $[LiFSI]_1[EC]_2$ electrolytes with 3DOM PI and 3DOM PI+PBI separators.

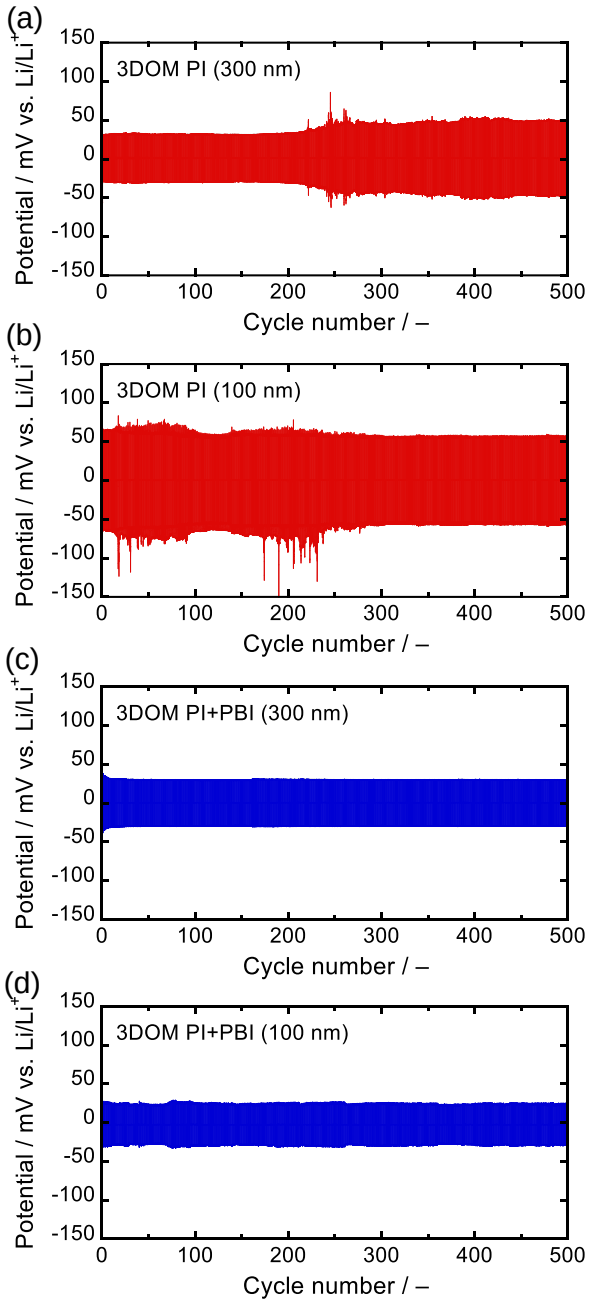

Figure 4–6. Voltage profiles of Li/Li symmetric cells employing (a) 3DOM PI (300 nm), (b) 3DOM PI (100 nm), (c) 3DOM PI+PBI (300 nm), and (d) 3DOM PI+PBI (100 nm) separators measured at 10 mA cm^{-2} for 30 min.

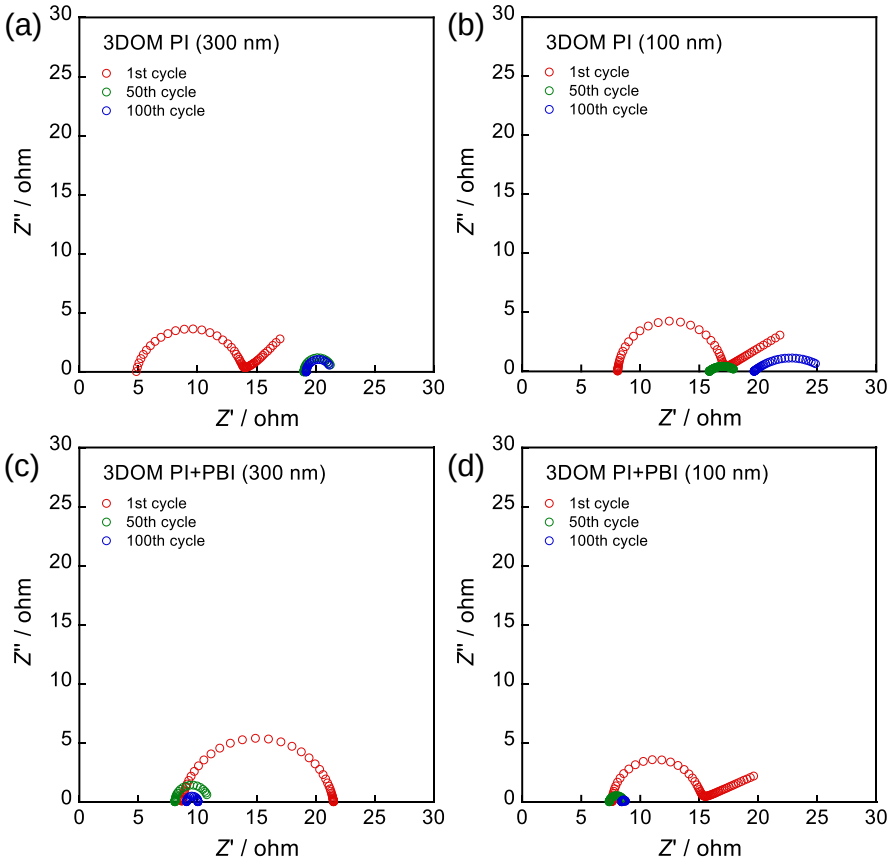

Figure 4–7. Cole–Cole plots during Li deposition/dissolution cycles in Li/Li symmetric cells employing (a) 3DOM PI (300 nm), (b) 3DOM PI (100 nm), (c) 3DOM PI+PBI (300 nm), and (d) 3DOM PI+PBI (100 nm) separators after the 1st, 50th, and 100th cycles.

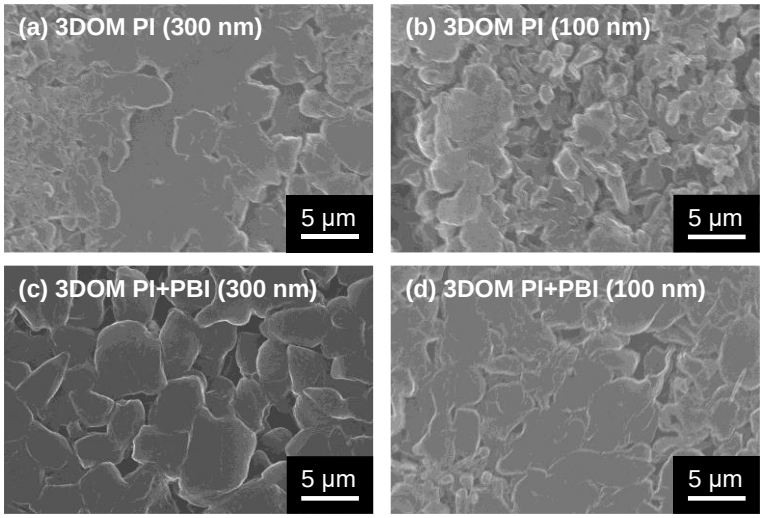

Figure 4–8. SEM images of deposited Li metal surface in Li/Li symmetric cells employing (a) 3DOM PI (300 nm), (b) 3DOM PI (100 nm), (c) 3DOM PI+PBI (300 nm), and (d) 3DOM PI+PBI (100 nm) separators after the 100th cycle.

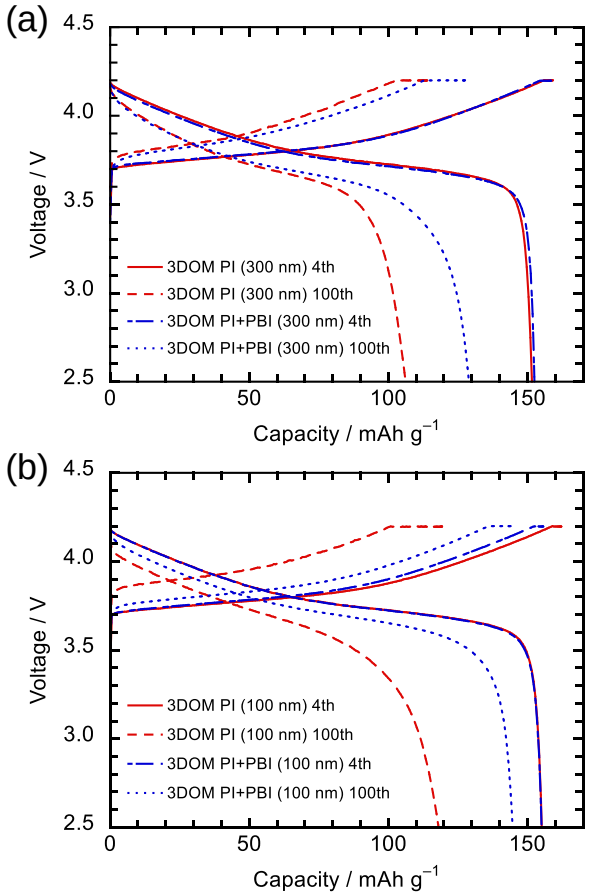

Figure 4–9. Charge–discharge curves of NCM523/Li full cells employing 3DOM PI and 3DOM PI+PBI separators with a pore size of (a) 300 nm and (b) 100 nm at 4th and 100th cycles.

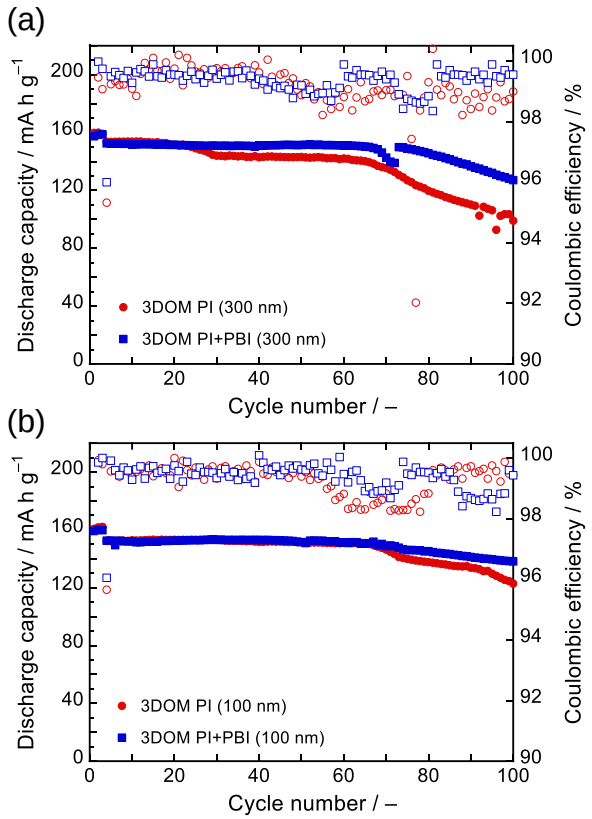

Figure 4–10. Discharge capacity and coulombic efficiency of NCM523/Li full cells employing 3DOM PI and 3DOM PI+PBI separators with a pore size of (a) 300 nm and (b) 100 nm.

4.5. References

1. J. M. Tarascon and M. Armand, Nature, 414, 359 (2001)
2. D. C. Lin, Y. Y. Liu, and Y. Cui, Nat. Nanotechnol., 12, 194 (2017)
3. P. Albertus, S. Babinec, S. Litzelman, and A. Newman, Nat. Energy, 3, 16 (2018)
4. J. Liu, Z. N. Bao, Y. Cui, E. J. Dufek, J. B. Goodenough, P. Khalifah, Q. Y. Li, B. Y. Liaw, P. Liu, A. Manthiram, Y. S. Meng, V. R. Subramanian, M. F. Toney, V. V. Viswanathan, M. S. Whittingham, J. Xiao, W. Xu, J. H. Yang, X. Q. Yang, and J. G. Zhang, Nat. Energy, 4, 180 (2019)
5. K. Kanamura, S. Shiraishi, and Z. Takehara, J. Electrochem. Soc., 143, 2187 (1996)
6. X. B. Cheng, R. Zhang, C. Z. Zhao, F. Wei, J. G. Zhang, and Q. Zhang, Adv. Sci., 3, 1500213 (2016)
7. H. P. Wu, H. Jia, C. M. Wang, J. G. Zhang, and W. Xu, Adv. Energy Mater., 11 (2021)
8. S. Park, R. Chaudhary, S. A. Han, H. Qutaish, J. Moon, M. S. Park, and J. H. Kim, Energy Mater., 3 (2023)
9. Y. Yamada, J. H. Wang, S. Ko, E. Watanabe, and A. Yamada, Nat. Energy, 4, 269 (2019)
10. D. Rakov, M. Hasanpoor, A. Baskin, J. W. Lawson, F. Chen, P. V. Cherepanov, A. N. Simonov, P. C. Howlett, and M. Forsyth, Chem. Mater., 34, 165 (2021)
11. Y. Maeyoshi, K. Yoshii, and H. Sakaebe, Electrochemistry, 90 (2022)
12. S. Shiraishi, K. Kanamura, and Z. Takehara, J. Appl. Electrochem., 25, 584 (1995)
13. K. Kanamura, S. Shiraishi, and Z. Takehara, J. Fluorine Chem., 87, 235 (1998)

14. R. Mogi, M. Inaba, S. K. Jeong, Y. Iriyama, T. Abe, and Z. Ogumi, J. Electrochem. Soc., 149, A1578 (2002)

15. N. Piao, S. F. Liu, B. Zhang, X. Ji, X. L. Fan, L. Wang, P. F. Wang, T. Jin, S. C. Liou, H. C. Yang, J. J. Jiang, K. Xu, M. A. Schroeder, X. M. He, and C. S. Wang, ACS Energy Lett., 6, 1839 (2021)

16. F. Hao, A. Verma, and P. P. Mukherjee, J. Mater. Chem. A, 6, 19664 (2018)

17. C. Hou, J. H. Han, P. Liu, C. C. Yang, G. Huang, T. Fujita, A. Hirata, and M. W. Chen, Adv. Energy Mater., 9 (2019)

18. S. Kanamori, M. Matsumoto, S. Taminato, D. Mori, Y. Takeda, H. J. Hah, T. Takeuchi, and N. Imanishi, RSC Advances, 10, 17805 (2020)

19. C. C. Fang, B. Y. Lu, G. Pawar, M. H. Zhang, D. Y. Cheng, S. R. Chen, M. Ceja, J. M. Doux, H. Musrock, M. Cai, B. Liaw, and Y. S. Meng, Nat. Energy, 6, 987 (2021)

20. X. Shen, R. Zhang, P. Shi, X. Chen, and Q. Zhang, Adv. Energy Mater., 11 (2021)

21. M. Eftekharnia, M. Hasanpoor, M. Forsyth, R. Kerr, and P. C. Howlett, ACS Appl. Energy Mater., 2, 6655 (2019)

22. J. Jang, J. Oh, H. Jeong, W. Kang, and C. Jo, Materials, 13 (2020)

23. H. Munakata, D. Yamamoto, and K. Kanamura, Chem. Commun., 3986 (2005)

24. K. Kanamura, T. Mitsui, and H. Munakata, Chem. Mater., 17, 4845 (2005)

25. D. Yamamoto, H. Munakata, and K. Kanamura, J. Electrochem. Soc., 155, B303 (2008)

26. H. Munakata, D. Yamamoto, and K. Kanamura, J. Power Sources, 178, 596 (2008)

27. Y. Maeyoshi, D. Ding, M. Kubota, H. Ueda, K. Abe, K. Kanamura, and H. Abe, ACS Appl. Mater. Interfaces, 11, 25833 (2019)

28. D. Kim, H. Munakata, J. Park, Y. Roh, D. Jin, M. H. Ryou, K. Kanamura, and Y. M. Lee, ACS Appl. Energy Mater., 3, 3721 (2020)

29. Y. Shimizu and K. Kanamura, J. Electrochem. Soc., 166, A754 (2019)

30. M. Nagasaki and K. Kanamura, ACS Appl. Energy Mater., 2, 3896 (2019)

31. J. Takeyoshi, N. Kobori, and K. Kanamura, Electrochemistry, 88, 540 (2020)

32. R. Miyagawa, J. Takeyoshi, K. Kanamura, S. Taminato, D. Mori, and N. Imanishi, Electrochemistry, 90 (2022)

33. P. G. Bruce and C. A. Vincent, J. Electroanal. Chem. Interfacial Electrochem., 225, 1 (1987)

34. P. G. Bruce, Solid State Ionics, 28-30, 918 (1988)

35. J. Evans, C. A. Vincent, and P. G. Bruce, Polymer, 28, 2324 (1987)

36. V. Mauro, A. D'Aprano, F. Croce, and M. Salomon, J. Power Sources, 141, 167 (2005)

37. C. F. J. Francis, I. L. Kyratzis, and A. S. Best, Adv. Mater., 32 (2020)

Chapter 5: Application of Al-LLZO Solid Electrolyte and Highly Concentrated Electrolytes for Lithium-Sulfur Cell

5.1. Introduction

The sulfur (S) cathode material possesses a significantly higher capacity density of 1672 mAh g^{-1} than that of conventional lithium-ion batteries, making it an attractive choice for high-energy-density rechargeable batteries. Furthermore, S is abundantly available and cost-effective. Consequently, there has been substantial research and development directed towards the advancement of lithium-sulfur (Li-S) batteries.[1–9] In this context, the fundamental processes of discharge and charge of S have been extensively investigated to realize high electrochemical performance of S as cathode material. During the discharge process of elemental Sulfur (S_8), it undergoes reduction to form Li_2S, passing through intermediate stages, including Li_2S_8, Li_2S_6, and Li_2S_2. Notably, these intermediates, along with S_8 and Li_2S, are characterized as electronically and ionically non-conductive materials. To facilitate the electrochemical reactions involving S, it is necessary to incorporate conductive materials within the S-cathode layer, thereby establishing an electronically conductive matrix.[10–17] Another important issue is the dissolution of intermediate species during the electrochemical reduction of S. It is well known that Li_2S_8 and Li_2S_6 tend to dissolve into non-aqueous electrolytes, which have traditionally been used in conventional Li-ion batteries. These dissolved intermediates migrated towards the Li-metal anode and reacted with the Li-metal. This results in a chemical self-discharge of the intermediates, posing a significant obstacle that must be

addressed to realize the full potential of Li-S batteries.[18–25] Notably, the conductivity of the cathode layer can be improved using carbon (C)-materials, such as Ketjen Black (KB), as discussed in previous research.[10–17]

In this study, the effects of chemical self-discharge were avoided by using new electrolytes. Previous reports have indicated that electrolytes based on sulfolane (SL) solvent or solvate ionic liquids suppress the dissolution of discharge intermediates.[23–25] In this study, liquid electrolytes were employed in the C/S cathodes. Furthermore, aluminum (Al)-doped $Li_7La_3Zr_2O_{13}$ ($Li_{6.25}Al_{0.25}La_3Zr_2O_{13}$ (Al-LLZO)) was employed as the separator in the Li-S cell. Al-LLZO demonstrates a Li^+ ion conductivity of 10^{-4} S cm^{-1} and remains stable in the presence of Li-metal anodes.[26–28] Importantly, the solid electrolyte can prevent the chemical self-discharge. A combination of ionic liquid or SL-based electrolyte and Al-LLZO solid electrolyte was first studied to suppress the dissolution of discharge intermediates of S and completely prevent the chemical self-discharge phenomenon.

5.2. Experimental

5.2.1. Preparation of composite materials between C and S

S-cathode materials lack electronic conductivity, necessitating the use conductive support materials, such as fine C-powder. We employed C-materials, KB (EC-600D, Lion Specialty Chemicals Co., Ltd.), as starting materials of C/S. S (99.999 %, Wako) was mixed with each C-material in a 5:1 weight ratio. Each mixture then underwent 30 min of grinding, followed by heating at 155 °C for 12 h under a flow of nitrogen gas (N_2). The S-content in each C/S was evaluated using thermal gravimetry (TG).

5.2.2. Electrolytes

Lithium bis(trifluoromethanesulfonyl)imide (LiTFSI) and tetraglyme (G4) were mixed in a 1:1 molar ratio to prepare the solvate ionic liquid [Li(G4)]TFSI. LiTFSI and SL were mixed with 1:2 in a molar ratio to prepare the $[Li(SL)_2][TFSI]$ electrolyte.[23–25] These electrolytes were employed as liquid electrolytes. Al-LLZO pellets were used as the solid electrolyte separators. The Al-LLZO powder was provided by DAIICHI KIGENSO KAGAKU KOGYO Co., Ltd. It was pressed into a disc shape and then heated at 1100 °C for 24 h, following the procedure outlined in our previous reports.[29–31] The diameter and thickness of the Al-LLZO pellets were 14 mm and 0.5 mm, respectively.

5.2.3. Electrochemical evaluation

The composite electrode was prepared on an Al current collector. C/S, carboxymethylcellulose, and styrene butadiene rubber were mixed in a 90:3.3:6.7 weight ratio and dispersed in *N*-methyl pyrrolidone (NMP) to prepare a coating slurry for the C/S composite electrode. After coating the slurry onto the Al current collector, the cathode sheet was dried at 80 °C under a vacuum for 24 h. Subsequently, the cathode sheet was pressed to adjust the thickness of the electrode layer on the Al current collector. Two types of separators were utilized to electrochemically evaluate the three types of electrolytes. When using the [Li(G4)][TFSI] or $[Li(SL)_2][TFSI]$ liquid electrolytes, a glass filter (GA55, ADVANTES MFS, Inc.) was employed as the separator. When using the Al-LLZO solid electrolyte pellet, a three-dimensionally ordered macroporous polyimide (3DOM-PI) separator (20 μm) was attached to both the anode and cathode, as depicted in Figs. 5–1 (a) and (b).[32] This 3DOM-PI separator, in combination with a [Li(G4)][TFSI]

or [Li(SL)$_2$][TFSI] liquid electrolyte, served as an interlayer between the cathode or anode and the Al-LLZO solid electrolyte pellet to establish a stable and robust contact between the solid electrolyte and the cathode or anode layers.

The discharge and charge tests of each cell were conducted using discharge-charge equipment (TOSCAT-3100U, TOYO SYSTEM, Co., LTD.). These processes were performed at 60 °C within a potential range spanning from 1.3 to 3.5 V, with discharge and charge rates set at 0.1 C rate. A one minute interval was maintained between the discharge and charge. The C-rate was calculated from S weight in C/S and the theoretical capacity of 1672 mAh g^{-1}. The amount of S loading was 0.3 mg cm^{-2}. Following each discharge and charge cycle at a state of charge of 100 %, electrochemical impedance measurements were also conducted at 60 °C across a frequency range of 1 MHz to 0.1 Hz using an impedance analyzer (SP-200, BioLogic Science Instruments). All electrochemical measurements were executed using a 2032 type coin cell.

5.3. Results and discussion

Figures 5–2 (a) and (b) highlights the discharge and charge curves of Li-S cells with [Li(G4)][TFSI] and [Li(SL)$_2$][TFSI]. The polarization of the Li-S cell with [Li(G4)][TFSI] showcased significant improvement when employing the new C/S KB particles and composite electrodes with the 10 wt% KB additive. The electronic conductivity of the composite electrode increased with the addition of KB and C/S KB with a higher KB content. From these results, it can be concluded that the electronic conductive matrix plays a crucial role in the electrochemical kinetics of S-cathode materials. The discharge and charge behaviors of [Li(SL)$_2$][TFSI] closely resembled that of [Li(G4)][TFSI]. Over 5 cycles, the discharge capacities of Li-S cell with

[Li(G4)][TFSI] were 1276, 925, 864, 824, and 791 mAh g^{-1}, respectively. The corresponding values for $[Li(SL)_2][TFSI]$ were 984, 976, 944, 920, and 898 mAh g^{-1}, respectively. Notably, the degradation of the discharge capacity was evident when the [Li(G4)][TFSI] electrolyte was employed but improved with $[Li(SL)_2][TFSI]$. It is well known that the discharge products of S dissolve into the electrolyte, leading to the chemical self-discharge phenomenon. The solubility of the discharge products in $[Li(SL)_2][TFSI]$ was much lower than that in [Li(G4)][TFSI].[25] From these results, it can be observed that the lower solubility of the discharge products in the electrolyte is a key issue when suppressing the degradation of Li-S cells. Another interesting point is the initial discharge capacity of the Li-S cells. A higher discharge capacity, obtained using the [Li(G4)][TFSI] electrolyte, corresponds to a higher utilization of S in the composite electrode. While the electronic conductivity of the composite electrode did not depend on the type of electrolyte, the ionic conductivity was strongly influenced by the electrolyte. The ionic conductivity of $[Li(SL)_2][TFSI]$ was lower than that of [Li(G4)][TFSI]. Thus, a higher ionic conductivity of the electrolyte is necessary to obtain high utilization of S_8.

Figures 5–3 (a) and (b) illustrated the Nyquist plots of the Li-S cell using [Li(G4)][TFSI] or $[Li(SL)_2][TFSI]$ over five cycles. The interfacial impedance of the Li-S cells increased over the cycles, and the total impedance of the Li-S cell with $[Li(SL)_2][TFSI]$ was higher than that of the Li-S cell with [Li(G4)][TFSI]. In contrast, the discharge potential profiles exhibited slightly less polarization for the Li-S cell with $[Li(SL)_2][TFSI]$, as shown in Figs. 5–2 (a) and (b). This is a unique result and may be influenced by the different solubilities of the discharge products in the two electrolytes. A lower solubility of the discharge intermediates leads to a quicker deposition of final discharge products when the discharge process proceeds via a dissolution/deposition

mechanism. The electrochemical impedance of the composite electrode is influenced by the ionic conductivity of the electrolyte. The potential profile at a constant current for the dissolution/deposition process depends not only on the ionic conductivity of the electrolyte, but also on the solubility of the reaction intermediates in the electrolyte. A more detailed explanation remains a subject for in future studies.

Furthermore, Al-LLZO pellets were employed to prevent chemical self-discharge of the intermediate products. The discharge–charge curves are shown in Figs. 5–4 (a) and (b). Higher discharge capacities were obtained for both cell types. The discharge capacities of the Li-S cell with [Li(G4)][TFSI] were 1408, 1391, 1355, 1319, and 1282 mAh g^{-1} over five cycles, and those of the Li-S cell with $[Li(SL)_2][TFSI]$ were 1475,1382, 1323, 1277, and 1241 mAh g^{-1}, respectively. Different discharge behaviors were observed for the two Li-S cells with [Li(G4)][TFSI] and $[Li(SL)_2][TFSI]$, but both Li-S cells with Al-LLZO solid electrolyte pellets exhibited similar behavior. This result indicated that the Al-LLZO solid electrolyte effectively suppressed the chemical self-discharge phenomenon of the discharge intermediates. However, the introduction of Al-LLZO increased the polarization during the discharge and charge of S. The discharge capacities of both the cell types were almost equal to the theoretical discharge capacity of S (1672 mAh g^{-1}). This indicates that the suppression of the self-discharge phenomenon of the discharge intermediates is more important to obtain better performance of the S-cathode.

Figures 5–5 (a) and (b) presents the Nyquist plots for the Li-S cells with the Al-LLZO pellet and the liquid electrolytes [Li(G4)][TFSI] or $[Li(SL)_2][TFSI]$. The total electrochemical impedance increased with the discharge and charge cycling in both cells. This impedance change may be attributed to cathode degradation. This was because the

chemical self-discharge phenomenon of the discharge intermediates was avoided in the presence of the Al-LLZO solid electrolyte pellet. For the Li-S cell with [Li(G4)][TFSI], two semicircles were observed, which differ from those observed for $[Li(SL)_2][TFSI]$. As discussed above, the solubility of the sulfides such as the discharge intermediates and S-materials in [Li(G4)][TFSI] was higher than that in $[Li(SL)_2][TFSI]$. During discharging, the sulfides dissolved in the electrolyte and reacted with the surface of the Al-LLZO solid electrolyte pellet to form a resistive layer consisting of reaction products between the surface impurities of Al-LLZO and the sulfides. If such an interlayer is formed on the Al-LLZO surface, an additional semicircle can be observed. The coulombic efficiencies of the two cells were estimated as 97 and 98 %, respectively. These high coulombic efficiencies were due to the Al-LLZO solid electrolyte separator.

The rate capabilities of the two cells were determined, as shown in Figs. 5–6 (a) and (b). The rate capability of the Li-S cell with $[Li(SL)_2][TFSI]$ and Al-LLZO was better than that of the Li-S cell with [Li(G4)][TFSI] and Al-LLZO. The discharge capacity of 1000 mAh g^{-1} was obtained even at 1.0 C rate. The rate capabilities expected from the electrochemical impedance of the two cells differed from the obtained results. As discussed above, the dissolution/deposition mechanism strongly depends on the solubility of the intermediate species Li_2S_8 and Li_2S_6 during the discharge process. When the solubility is very low, the intermediates are quickly supersaturated and deposited on the C-current collector during the constant current discharge, leading to faster S-kinetics. This is a possible explanation for the unique polarization behavior. More detailed research is required to understand this unique behavior.

Figure 5–6 (c) show the changes in the discharge capacity over 50 cycles. The Li-S cell with $[Li(SL)_2][TFSI]$ and Al-LLZO exhibited 800 mAh g^{-1} discharge capacity

and 90 % coulombic efficiency even after 50 cycles. The performance of the Li-S cell was significantly improved using the Al-LLZO pellet and $[Li(SL)_2][TFSI]$ electrolytes. However, the discharge capacity decreased with cycling. This degradation may be due to the loss of electronic conductivity of the cathode layer caused by the volume change of the electrode (S_8) during the discharge and charge cycles. Another possible mechanism is the formation of a surface layer on the Al-LLZO solid electrolyte caused by the chemical reactions of Al-LLZO with the discharge intermediates. Based on the electrochemical impedance results, the volume change of the composite electrode is a more probable reason for cell degradation. The detailed mechanisms should be clarified to improve the cycleability of Li-S cells in the future.

5.4. Conclusion

Two types of electrolytes were employed to investigate the effect of the solubility of the discharge intermediates on the discharge behavior of Li-S cells. $[Li(SL)_2][TFSI]$, which has a lower solubility and exhibited better Li-S cell performance. The application of the Al-LLZO solid electrolyte pellet also improved the cell performance. In particular, the chemical self-discharge phenomenon was suppressed by the solid electrolyte separator. As a result, the coulombic efficiency was significantly improved.

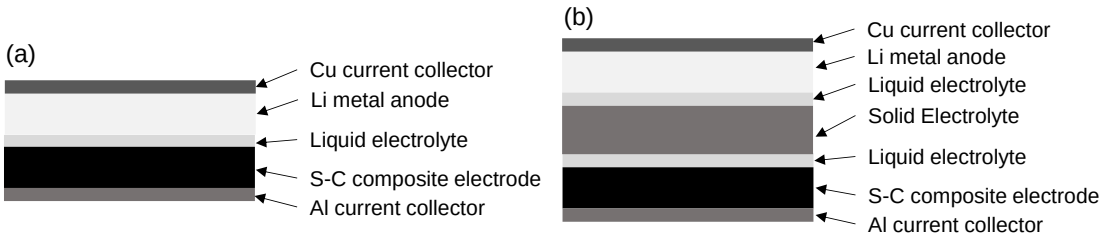

Figure 5–1. Schematic illustration of Li-S cells, (a) C/S composite electrode/liquid electrolyte + GA55/Li metal anode, and (b) C/S composite electrode/liquid electrolyte + 3DOM PI separator/Al-LLZO/liquid electrolyte + 3DOM PI separator/Li metal anode, liquid electrolytes: [Li(G4)][TFSI] or $[Li(SL)_2][TFSI]$, cell: 2032 type coin cell.

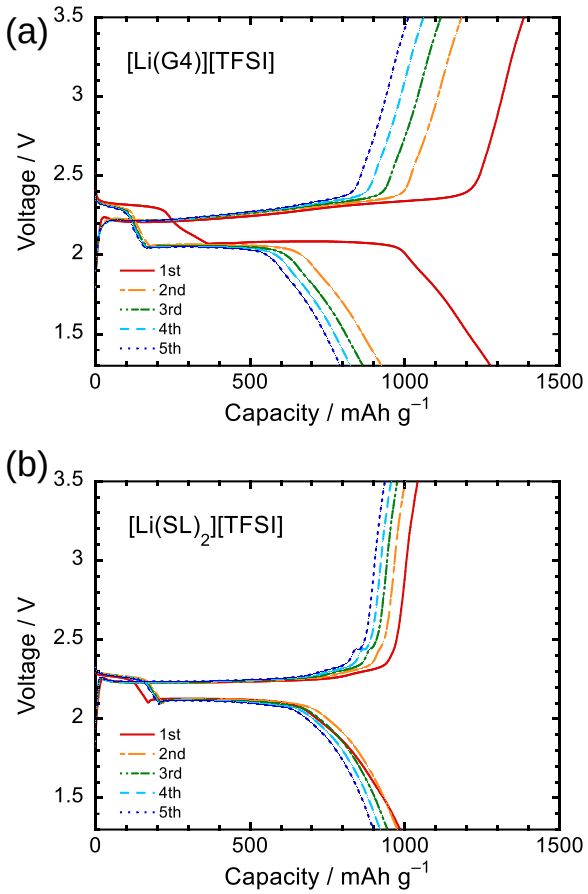

Figure 5–2. Discharge and charge curves of Li-S cells with (a) [Li(G4)][TFSI] and (b) $[Li(SL)_2][TFSI]$ at 60 °C and 0.1 C rate.

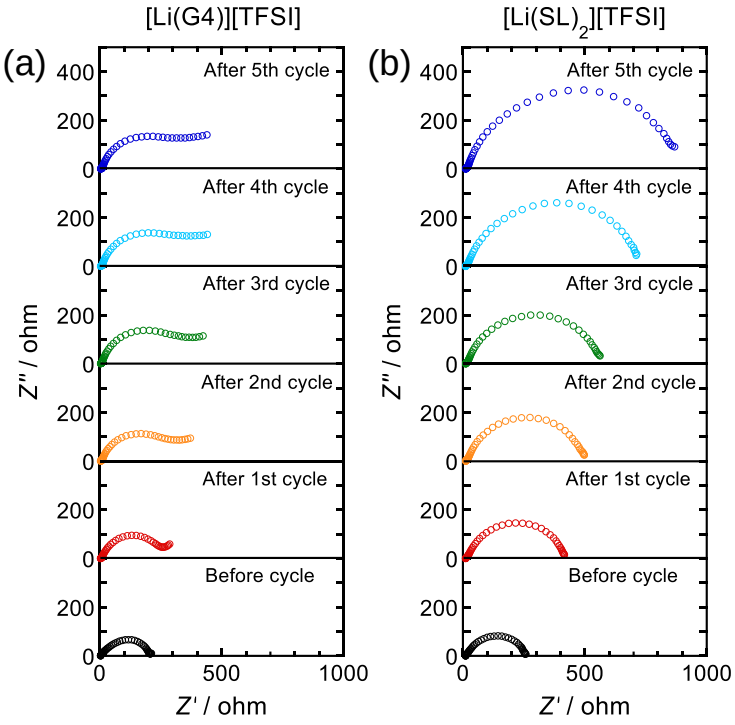

Figure 5–3. Nyquist plots of Li-S cells with (c) [Li(G4)][TFSI] and (d) $[Li(SL)_2][TFSI]$ at 60 °C during 5 cycles.

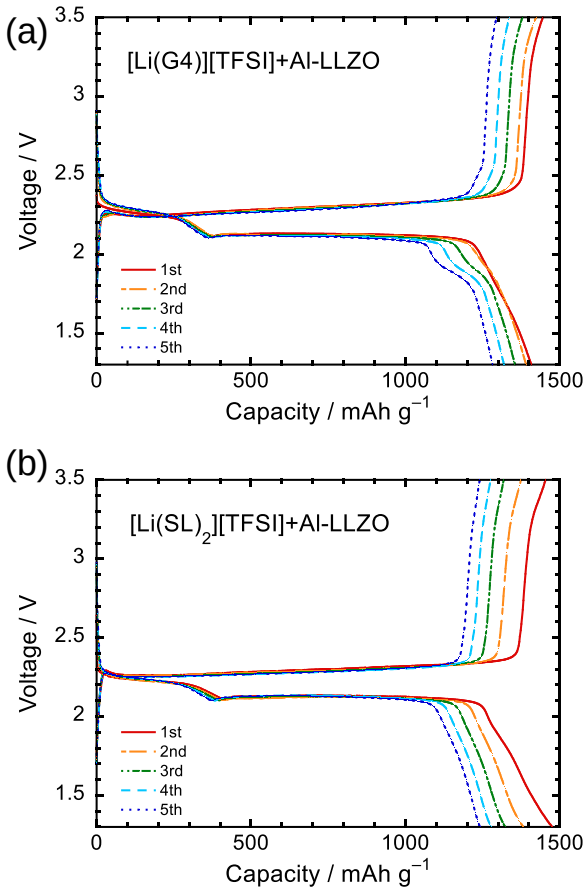

Figure 5–4. Discharge and charge curves of Li-S cells with (a) [Li(G4)][TFSI] electrolyte + Al-LLZO pellet and (b) $[Li(SL)_2][TFSI]$ electrolyte + Al-LLZO pellet at 60 °C and 0.1 C rate.

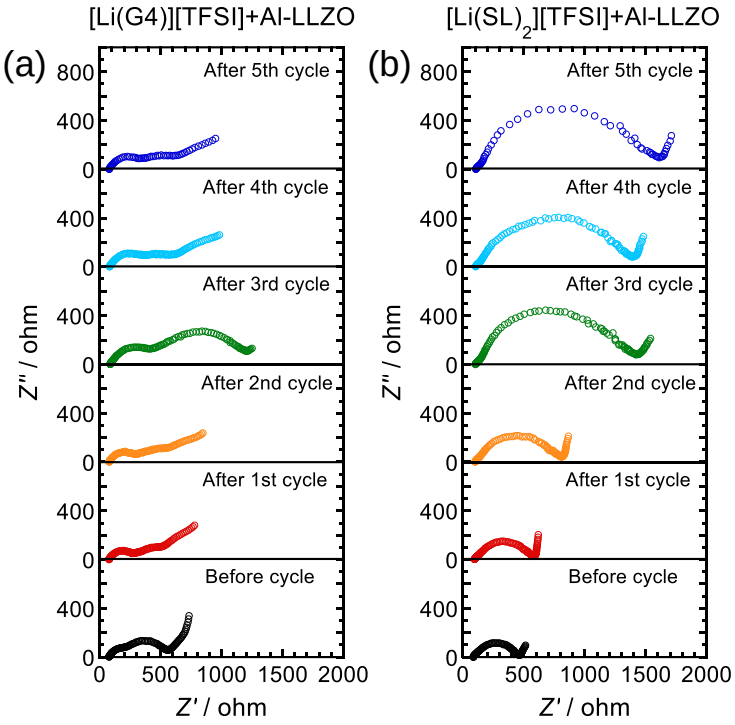

Figure 5–5. Nyquist plots of the Li-S cells with (c) [Li(G4)][TFSI] electrolyte + Al-LLZO pellet and (d) $[Li(SL)_2][TFSI]$ electrolyte + Al-LLZO pellet at 60 °C.

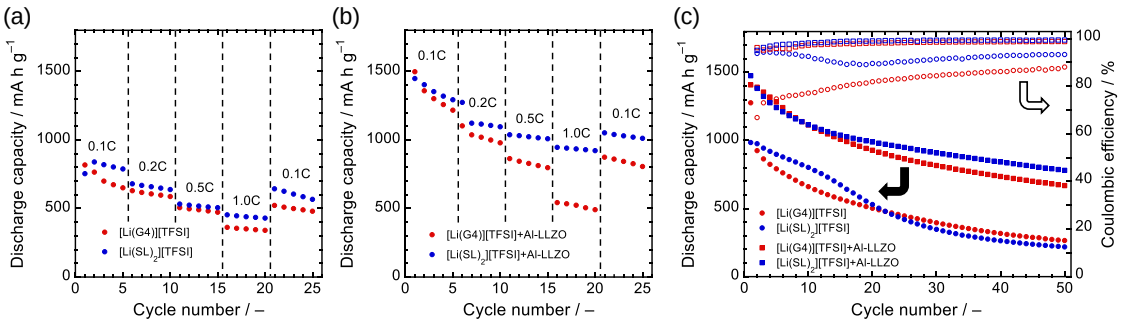

Figure 5–6. Rate capabilities of Li-S cells at 60 °C (a) without Al-LLZO pellet (b) with Al-LLZO pellets. (c) Discharge capacity and changes of Li-S cells with [Li(G4)][TFSI] electrolyte, [Li(SL)$_2$][TFSI] electrolyte, [Li(G4)][TFSI] electrolyte + Al-LLZO pellets, and [Li(SL)$_2$][TFSI] electrolyte + Al-LLZO pellets at 60 °C and 0.1 C during 50 cycles.

5.5. References

1. S. Kim, Y. Jung, and S. J. Park, Electrochim. Acta, 52, 2116 (2007)
2. C. D. Liang, N. J. Dudney, and J. Y. Howe, Chem. Mater., 21, 4724 (2009)
3. M. Nagao, A. Hayashi, and M. Tatsumisago, J. Mater. Chem., 22, 10015 (2012)
4. N. S. A. Manan, L. Aldous, Y. Alias, P. Murray, L. J. Yellowlees, M. C. Lagunas, and C. Hardacre, J. Phys. Chem. B, 115, 13873 (2011)
5. S. S. Zhang, J. Power Sources, 231, 153 (2013)
6. X. L. Ji, and L. F. Nazar, J. Mater. Chem., 20, 9821 (2010)
7. J. R. Akridge, Y. V. Mikhaylik, and N. White, Solid State Ionics, 175, 243 (2004)
8. Q. J. Shao, S. D. Zhu, and J. Chen, Nano Res., 16, 8097 (2023)
9. X. H. Zhao, G. Cheruvally, C. Kim, K. K. Cho, H. J. Ahn, K. W. Kim, and J. H. Ahn, J. Electrochem. Sci. Technol., 7, 97 (2016)
10. B. Zhang, C. Lai, Z. Zhou, and X. P. Gao, Electrochim. Acta, 54, 3708 (2009)
11. C. Lai, X. P. Gao, B. Zhang, T. Y. Yan, and Z. Zhou, J. Phys. Chem. C, 113, 4712 (2009)
12. L. W. Ji, M. M. Rao, H. M. Zheng, L. Zhang, Y. C. Li, W. H. Duan, J. H. Guo, E. J. Cairns, and Y. G. Zhang, J. Am. Chem. Soc., 133, 18522 (2011)
13. Y. X. Yin, S. Xin, Y. G. Guo, and L. J. Wan, Angew. Chem. Int. Ed., 52, 13186 (2013)
14. A. Manthiram, S. H. Chung, and C. X. Zu, Adv. Mater., 27, 1980 (2015)
15. J. Schuster, G. He, B. Mandlmeier, T. Yim, K. T. Lee, T. Bein, and L. F. Nazar, Angew. Chem. Int. Ed., 51, 3591 (2012)
16. A. Eftekhari, and D. W. Kim, J. Mater. Chem. A, 5, 17734 (2017)
17. L. Djuandhi, U. Mittal, N. Sharma, and H. L. Andersen, J. Electrochem. Soc.,

170 (2023)

18. J. W. Park, K. Ueno, N. Tachikawa, K. Dokko, and M. Watanabe, J. Phys. Chem. C, 117, 20531 (2013)

19. Y. V. Mikhaylik, and J. R. Akridge, J. Electrochem. Soc., 151, A1969 (2004)

20. Z. Yuan, H. J. Peng, T. Z. Hou, J. Q. Huang, C. M. Chen, D. W. Wang, X. B. Cheng, F. Wei, and Q. Zhang, Nano Lett., 16, 519 (2016)

21. H. Al Salem, G. Babu, C. V. Rao, and L. M. R. Arava, J. Am. Chem. Soc., 137, 11542 (2015)

22. T. Nakazawa, A. Ikoma, R. Kido, K. Ueno, K. Dokko, and M. Watanabe, J. Power Sources, 307, 746 (2016)

23. S. Seki, N. Serizawa, K. Takei, Y. Umebayashi, S. Tsuzuki, and M. Watanabe, Electrochemistry, 85, 680 (2017)

24. T. Tonoya, H. Yamamoto, Y. Matsui, H. Hinago, and M. Ishikawa, Electrochemistry, 90 (2022)

25. K. Dokko, N. Tachikawa, K. Yamauchi, M. Tsuchiya, A. Yamazaki, E. Takashima, J. W. Park, K. Ueno, S. Seki, N. Serizawa, and M. Watanabe, J. Electrochem. Soc., 160, A1304 (2013)

26. J. Schwenzel, V. Thangadurai, and W. Weppner, J. Power Sources, 154, 232 (2006)

27. C. S. Nimisha, K. Y. Rao, G. Venkatesh, G. M. Rao, and N. Munichandraiah, Thin Solid Films, 519, 3401 (2011)

28. S. L. Zhao, Z. W. Fu, and Q. Z. Qin, Thin Solid Films, 415, 108 (2002)

29. R. Murugan, V. Thangadurai, and W. Weppner, Angew. Chem. Int. Ed., 46, 7778 (2007)

30. Y. Matsuda, K. Sakamoto, M. Matsui, O. Yamamoto, Y. Takeda, and N. Imanishi, Solid State Ionics, 277, 23 (2015)

31. M. Kotobuki, K. Kanamura, Y. Sato, and T. Yoshida, J. Power Sources, 196, 7750 (2011)

32. M. Nagasaki, and K. Kanamura, ACS Appl. Energy Mater., 2, 3896 (2019)

Chapter 6: General conclusions

In this study, the highly-concentrated electrolytes and 3DOM separators for Li-metal anode were investigated.

In Chapter 2, a 3DOM PI separator was proposed as a high-affinity separator for highly concentrated ILE. Both the affinity for ILE and the electrochemical properties of the 3DOM PI separator were investigated and compared with those of conventional surfactant-coated PP separators. The 3DOM PI separator comprised polyimide and exhibited high porosity and a 3D-ordered pore structure. These properties provided a better affinity for highly concentrated ILE and higher ionic conductivity than those of the surfactant-coated PP separator. The higher ionic conductivity of the 3DOM PI separator with ILE provided a higher maximum current density of Li metal deposition/dissolution for Li/Li symmetric cells and a higher rate capability for the NCM523/Li full cell. These observations indicate that the ionic conductivity of highly concentrated ILE in the separators significantly affects their rate capabilities. Moreover, the Li/Li symmetric cell and NCM523/Li full cell with the 3DOM PI separator provided more stable internal resistance and cycle performance than those with the surfactant-coated PP separator. Because the chemical composition of the SEI layer on the Li metal surface was almost the same between surfactant-coated PP and 3DOM PI separator, the morphology of the deposited Li metal was an important factor determining the cycle performance of the cells. The 3D-ordered uniform pore structure of the 3DOM PI separator provided a non-dendritic Li metal deposition morphology, resulting in high coulombic efficiency and high cycle stability.

In Chapter 3, the surfactant-coated PP and 3DOM PI separators were introduced as a framework for the IG electrolyte. The separator improved the mechanical strength of the IG electrolyte membrane, and the self-standing membranes were successfully prepared. The improvement of the mechanical strength suppressed an internal short circuit owing to the nonuniform Li deposition/dissolution behavior. In particular, the 3DOM PI–IG composite electrolyte membrane exhibited highly stable Li deposition/dissolution behavior. The NCM523/Li full cell with the 3DOM PI–IG composite electrolyte exhibited higher coulombic efficiency and cycle performance. The high porosity and uniform porous structure of the 3DOM PI separator provided higher conductance of the electrolyte layer, leading to more uniform Li deposition/dissolution behavior owing to more uniform interface formation between Li metal and electrolyte. The composite of the 3DOM PI separator and IG electrolyte was useful to improve the trade-off relationship between ionic conductivity and mechanical strength of the IG self-standing membrane.

In Chapter 4, PBI was added to a 3DOM PI separator to increase its mechanical strength. Four types of separators were prepared using two materials, PI and PI+10 wt% PBI, and two types of template particles, 300 and 100 nm, and their physical and electrochemical properties are also investigated. The 3DOM PI separator exhibited a higher porosity and Gurley number, while the 3DOM PI+PBI separator exhibited higher tensile strength and thermal stability. Furthermore, the 3DOM PI+PBI separator showed a more stable Li deposition/dissolution and charge–discharge cycle performance of the full cell than the 3DOM PI separator. An increase in the mechanical strength of the separator prevented the compression of pores in the separator by external pressure, and provided a more uniform reaction distribution in the electrodes. The pore size of the

3DOM PI+PBI separators also affected the size of granular Li. The 3DOM PI+PBI (100 nm) separator provided smaller granular Li but a more uniform electrode reaction distribution, which resulted in better charge–discharge cycle performance of the full cell.

In Chapter5, two types of electrolytes were employed to investigate the effect of the solubility of the discharge intermediates on the discharge behavior of Li-S cells. $[Li(SL)_2][TFSI]$ has a lower solubility of discharge intermediates and exhibited better Li-S cell performance. The application of the Al-LLZO solid electrolyte pellet also improved the cell performance. In particular, the chemical self-discharge phenomenon was suppressed by the solid electrolyte separator, and the coulombic efficiency was significantly improved.

List of publication

1. Y. Shimbori, K. Nishikawa, K. Kajihara, K. Kanamura, Application of 3DOM PI Separator to Li Metal Battery with Highly Concentrated Ionic Liquid Electrolyte, Electrochemistry, 91, 127003 (2023).

2. Y. Shimbori, K. Kajihara, K. Kanamura, Improvement of the Electrochemical Performances of Li-Metal Anode by Composite of Ion Gel Electrolyte and Three-Dimensionally Ordered Macroporous Polyimide Separator, (to be submitted).

3. Y. Shimbori, S. Ooga, K. Kajihara, K. Kanamura, Effect of Polybenzimidazole Addition to Three-Dimensionally Ordered Macroporous Polyimide Separators on Mechanical Properties and Electrochemical Performances, Electrochemistry, 92, 027008 (2024).

4. S. Oho, Y. Shimbori, K. Kanamura, Optimization of Carbon/Sulfur Composite and Application of Al-LLZO Solid Electrolyte and Highly Concentrated Electrolytes for Lithium-Sulfur Cell, Electrochemistry, 92, 017001 (2024).